O-GlcNAc transferase acts as a critical nutritional node for the control of liver homeostasis

Paula Ortega-Prieto, Lucia Parlati, Fadila Benhamed, Marion Regnier, Isadora Cavalcante, Mélanie Montabord, Rachel Onifarasoaniaina, Maryline Favier, Natasa Pavlovic, Julie Magusto, et al.

O-GlcNAc transferase acts as a critical nutritional node for the control of liver homeostasis

Paula Ortega-Prieto[1*], Lucia Parlati[1*], Fadila Benhamed[1], Marion Regnier[1], Isadora Cavalcante[2], Mélanie Montabord[1], Rachel Onifarasoaniaina[3], Maryline Favier[3], Natasa Pavlovic [4], Julie Magusto[5], Michèle Cauzac[1], Patrick Pagesy[1], Jérémie Gautheron[5], Chantal Desdouets[4], Sandra Guilmeau[1], Tarik Issad[1]# and Catherine Postic[1]#

[1]Université Paris Cité, Institut Cochin, CNRS, INSERM, Paris, France; [2] Team Genomics and signaling of endocrine tumors, Institut Cochin, CNRS, INSERM, Université Paris Cité, F-75014 PARIS, France ; [3]HistIM Platform, Institut Cochin, CNRS, INSERM, Université de Paris Cité, F- 75014 PARIS, France; [4]Team Proliferation, Stress and liver physiopathology, Centre de Recherche des Cordeliers, INSERM, Sorbonne Université, Université Paris Cité, F-75006 PARIS, France; [5]Centre de Recherche Saint-Antoine, Sorbonne Université, Inserm, Paris, France.

*These authors contributed equally
#Corresponding authors: catherine.postic@inserm.fr, tarik.issad@inserm.fr

Financial statements

P.O-P. was supported by the European Union's Horizon 2020 Research and Innovation Programme under the Marie Skłodowska-Curie Grant Agreement No 675610 (Current address: Drug Transport and Tumour Metabolism Lab, MRC London Institute of Medical Sciences, London, UK) and L.P was supported by AFEF (Association Française pour l'Etude du Foie) and by INSERM (Poste d'accueil). C.P. acknowledges the support of grants from the National Agency for Research (ANR) (ANR-20-CE14-0038 IMAGINE; ANR-20-CE14-HEPATOMORPHIC, ANR RHU QUID NASH).

Data Availability Statement: Data sharing subject to agreement.

Abbreviations: ALT, alanine aminotransferase; ALP, alkaline phosphatase; ARE, antioxidant response element; AST, aspartate aminotransferase; βOHB, β hydoxybutyrate; Ccl5, C-C motif chemokine ligand 5; CHOP, CCAAT-enhancer-binding protein homologous protein; Col3a1, collagen type III alpha 1 chain; Col6a1, collagen type VI alpha 1 chain; CV, central vein; Cxcl1, C-X-C motif chemokine ligand 1; Cyc, cyclin; DDB1, damage specific DNA binding protein 1; DE genes, differentially expressed genes; EZH, enhancer of zeste homolog; FDR, false discovery rate; Foxo1, Forkhead box protein o1; G6Pase, Glucose-6-phosphate dehydrogenase; GAPDH, glyceraldehyde 3-phosphate dehydrogenase; GSH, reduced glutathione; GSSG, oxidized glutathione; Gsta, glutathione S-transferase alpha; Gstm, glutathione S-transferase mu; H2A.X, H2A.X variant histone; HBP, hexosamine biosynthesis pathway; HE, hematoxylin eosin; HO1, heme oxygenase 1; HNF4α, hepatocyte nuclear factor 4α; IL-1β, interleukin-1β; JNK, c-Jun N-terminal kinase; Krt7/19, Cytokeratin 7/19; LDH, lactate dehydrogenase; MDA, malondialdehyde; MCP1, monocyte chemoattractant protein-1; MLKL, Mixed lineage kinase domain like pseudokinase; NAFLD, non-alcoholic fatty liver disease; NASH, non-alcoholic steatohepatitis; NqO1, NAD(P)H quinone dehydrogenase 1; NRF2, nuclear factor erythroid-derived 2-related factor ; OGA, O-GlcNAcase; OGT, O-GlcNAc transferase; PCNA, proliferating cell nuclear antigen; PEPCK, Phosphoenolpyruvate carboxykinase; PV, portal vein; RT-qPCR, quantitative reverse transcription PCR; RIPK3, Receptor-interacting serine/threonine-protein kinase 3, ROS, reactive oxygen species; αSMA, alpha-smooth muscle actin; SOX9, sex determining region Y-box 2; TBP, TATA-box binding protein; TGFβ, transforming growth factor β; TNFα, tumor necrosis factor alpha; TUNEL, Terminal deoxynucleotidyl transferase dUTP nick end labelling, WGA, wheat germ agglutinin; YAP, yes-associated protein.

Abstract

Background & Aims: O-GlcNAcylation is a reversible post-translational modification controlled by the activity of two enzymes, O-GlcNAc transferase (OGT) and O-GlcNAcase (OGA). In liver, O-GlcNAcylation has emerged as an important regulatory mechanism underlying normal liver physiology and metabolic disease.

Methods: To address whether OGT acts as a critical hepatic nutritional node, mice with a constitutive hepatocyte-specific deletion of OGT (OGT^{LKO}) were generated and challenged with different carbohydrate- and lipid-containing diets.

Results: Analyses of 4 week-old OGT^{LKO} mice revealed significant oxidative and ER stress, DNA damage, together with inflammation and fibrosis in liver. Susceptibility to oxidative and ER stress-induced apoptosis was also elevated in OGT^{LKO} hepatocytes. While OGT expression was partially recovered in liver of 8 week-old OGT^{LKO} mice, hepatic injury and fibrosis were not rescued but rather worsened with time. Interestingly, weaning of OGT^{LKO} mice on a ketogenic diet (low carbohydrate high fat), fully prevented the hepatic alterations induced by OGT deletion, indicating that reduced carbohydrate intake protects OGT deficient liver.

Conclusion: These findings pinpoint OGT as a key mediator of hepatocyte homeostasis and survival upon carbohydrate intake and validate OGT^{LKO} mice as a valuable model for assessing therapeutical approaches of advanced liver fibrosis.

Key words: OGT, oxidative stress, liver fibrosis, carbohydrate intake, ketogenic diet

Electronic word counts: 7497

Number of figures: 7

Number of tables: 0

Impact and implications

Our study shows that hepatocyte-specific deletion of O-GlcNAc transferase (OGT) leads to severe liver injury, reinforcing the importance of O-GlcNAcylation and OGT for hepatocyte homeostasis and survival. Our study also validates the *Ogt* liver deficient mouse as a valuable model for the study of advanced liver fibrosis. Importantly, since the severe hepatic fibrosis of *Ogt* liver deficient mice could be fully prevented upon feeding on a ketogenic diet (i.e. very low carbohydrate high fat diet) underlines the potential interest of nutritional intervention as anti-fibrogenic strategies.

Introduction

O-GlcNAcylation is a dynamic and reversible post-translational modification controlled by the activity of two enzymes, O-GlcNAc transferase (OGT) and O-GlcNAcase (OGA). OGT and OGA mediate the dynamic cycling of O-GlcNAcylation on a wide variety of cytosolic, nuclear and mitochondrial proteins, in response to environmental changes, such as nutrients or stress challenges (Yang and Qian, 2017). Therefore, O-GlcNAcylation has been proposed as a nutrient and stress sensor, that mediates cellular adaptations ranging from transcription and translation to signal transduction and metabolism. As a result, disruption of O-GlcNAc homeostasis has been implicated in the pathogenesis of several human diseases, including cancer, diabetes and neurodegeneration (Nie and Yi, 2019).

In the liver, O-GlcNAcylation has emerged as an important regulatory mechanism underlying normal liver physiology and metabolic disease. O-GlcNAcylation significantly contributes to liver gluco-lipotoxicity by modulating key effectors of hepatic metabolism (Guinez et al., 2011; Kuo et al., 2008). Moreover, OGT acts as a suppressor of hepatocyte necroptosis (a specific form of regulated cell death) and its hepatic deletion triggers liver fibrosis in mice (Zhang et al., 2019). Altogether, these studies suggested that OGT may act as a critical molecular switch between hepatocyte survival and death in response to chronic liver injury (Zhang et al., 2019).

While several cellular functions of O-GlcNAcylation are clearly emerging, we hypothesize that OGT loss of function may prevent liver cells to cope with the oxidative stress induced by dietary glucose (Du et al., 2010; Mohanty et al., 2000; de Carvalho Vidigal et al., 2012; Dickinson et al., 2008). Indeed, OGT was shown to protect against oxidative stress by promoting antioxidant responses, whereas lack of OGT correlates with high oxidative stress in response to elevated glucose concentrations (Chen et al., 2018). To test this hypothesis, we first examined at different time points ranging from 2 weeks to 1 year, the phenotype of mice with a constitutive OGT deficiency in hepatocytes (OGT^{LKO}) and fed a 70% carbohydrates diet. We

then explored whether limiting carbohydrate intake at weaning could protect the liver against lack of OGT. Interestingly, analysis of OGT^{LKO} mice at 4 weeks revealed the onset of hepatic oxidative and ER stress, DNA damage, together with liver inflammation and moderate fibrosis. Liver injury and fibrosis worsened with time when OGT^{LKO} mice were maintained on a high carbohydrate diet, as characterized by advanced hepatic fibrosis and septa surrounding regenerative nodules. Interestingly, weaning OGT^{LKO} mice on a ketogenic low carbohydrate (1%) high fat diet, to limit carbohydrate intake, fully prevented the severe hepatic alterations induced by early OGT deletion, including advanced fibrosis. These findings underline the critical role of OGT in hepatocytes homeostasis and survival upon carbohydrate intake. Our study also establishes the OGT^{LKO} mouse model as a spontaneous model of advanced fibrosis, that may, in the future, facilitate therapeutic target identification for prevention and treatment of chronic liver disease.

Material and methods

Generation of OGT^{LKO} mice

Conditional hepatic-specific OGT knock out mice (OGT^{LKO}) and control floxed littermates (OGT^{LWT}) were generated by crossing *Albumin-Cre; $Ogt^{F/Y}$* with *$Ogt^{F/F}$* mice. *The Ogt* locus was floxed on either side of the exons 6-7 encoding amino acids 206 and 232. *Ogt* mice were obtained from Jackson Laboratories (JAX stock #00486).

Animals and nutritional challenges

All animal procedures were carried out according to the French guidelines for the care and use of experimental animals (Animal authorization agreements #9723, #19226 and #33226 from University of Paris Ethical Committee). Mice (males and females) were housed in colony housing on a 12hr light/dark cycle. All mice were given free access to water and control chow diet (Standard diet (SD) in % of calories: 69% of carbohydrates, 4% of fat and 26% of proteins; SAFE #A03). Regarding nutritional challenges, OGT^{LWT} and OGT^{LKO} mice were weaning and fed for 5 weeks with a low carbohydrate high fat diet (LCHF in % of calories: 21% of carbohydrates, 60% of fat, 19% of proteins) (SSNIF #E15742) or a ketogenic diet (KD in % of calories: 1% of carbohydrates, 94% of fat, 5% of proteins) (SSNIF #E15149). The age and sex of the mice are specified in the results and figure legends.

Blood glucose concentrations and glucose homeostasis

Blood glucose was measured in total blood using an Accu-Check glucometer (Roche). Glucose tolerance tests (GTT), pyruvate tolerance tests (PTT) and insulin tolerance tests (ITT) were performed in 4 week-old OGT^{LKO} and control OGT^{LWT} littermates. For GTT, mice were fasted 4 to 5 hours and received 2g/kg of glucose; for PTT, mice were fasted overnight and received

1g/kg of pyruvate; for ITT, mice were fasted 4 to 5 hours and received 0.75U/kg of insulin. Blood glucose concentrations were measured over a period of 120 minutes for all tests.

β-hydroxybutyrate concentrations

β-Hydroxybutyrate was measured with Optium β-ketone test strips that carried Optium Xceed sensors (Abbott Diabetes Care).

Cytokines and liver enzymes concentrations

Concentrations of serum cytokines were analyzed using the V-PLEX proinflammatory panel 1 mouse kit (Mesoscale, K15048D). Serum alanine aminotransferase (ALT), aspartate aminotransferase (AST), lactate dehydrogenase (LDH), alkaline phosphatase (ALP) and total and direct bilirubin concentrations were determined using an automated Monarch device (Laboratoire de Biochimie, Faculté de Médecine Bichat, France).

RNA isolation, reverse transcription and qPCR

Snap frozen liver tissue was powdered and approximately 15mg of liver powder was used for RNA extraction using the SV Total RNA isolation system (Promega, Z3101). mRNAs were reverse transcribed and cDNA levels were measured by qPCR (LightCycler480 SYBR Green I Master, Roche) using the primers described in the Table S4. Gene expression was normalized over expression of the TATA-box binding protein (TBP) mRNA levels.

Protein extraction, western blot and wheat germ agglutinin (WGA) precipitation experiments

Whole tissue was lysed in lysis buffer (20mM Tris HCl [pH 7.5], 150mM NaCl, 5mM EDTA, 50mM NaF, 30mM NaP, 1% Triton X-100, EDTA free protease inhibitor cocktail [Roche, 4693132001], orthovanadate 1mM, Thiamet-G 10µM [Sigma, SML0244]). Western blot was performed using 30µg of lysate. For lectin-based precipitation assay, the lysate (1mg of

proteins) was incubated overnight with 25µL of WGA agarose beads (Sigma, L1882) at 4°C. The precipitate was resolved by SDS-PAGE and immunoblotted with specific antibodies. Antibodies used are the following: anti-OGT (Sigma, SAB4200311), anti-O-linked N-acetylglucosamine antibody (RL2, ab2739), anti-GAPDH (Santa Cruz, sc-25778), anti-β-actin (CST #4970), anti-CycA2 (Santa Cruz, sc-596), anti-CycD1 (CST #2978), anti-PCNA (CST #2586), anti-p62 (Enzo Life Sciences, BML-PW9860-0100), anti-p-p62 (CST #14354), anti-CHOP (CST #5554), anti-γH2AX (CST #2577), anti-H2AX total (CST #7631), anti-Cleaved Caspase-3 (CST #9661), anti-MLKL (ab172868), anti-RIPK3 (orb74415), anti-Foxo1 (CST #2880), Anti-JNK (CST #9252), anti p-JNK (CST#9255). Semi-quantitative analysis was performed using ChemiDoc software (Bio-rad).

Histological analyses and tissue staining

Fixed livers (4% PFA, 24h at 4ºC) were embedded in paraffin and sliced at 7µm. After deparaffinization and rehydration, slides were stained with hematoxylin-eosin (HE), Sirius red and αSMA for fibrosis detection. In the case of immunolabeling, antigen retrieval was performed in citrate buffer for 10 min at 95ºC and treated with peroxidase blocking reagent (Sigma, H1009). Slides were permeabilized with 0.01% Tween20 and unspecific antigenicity was blocked with 2% BSA and 2% serum, from the species in which the secondary antibody was raised. Primary antibodies used are the following: anti-OGT (Abcam, ab96718), anti-Ki67 (ThermoFisher, MA5-14520), anti-HNF4α (Santa Cruz, sc-6556), anti-SOX9 (EMD millipore, ab5535) and anti-Krt19 (Abcam, ab52625), anti-F4/80 (CST#70076), anti-MDA (Abcam, ab27642). Secondary antibodies HRP-conjugated were revealed by incubation with DAB substrate (Dako, K3468), co-stained with hematoxylin (Vector laboratories, H-3404) and mounted with VectaMount™ mounting medium (Vector laboratories, H-5000). For apoptosis, the TUNEL kit (EMD Millipore kit S71000) was used. Images analysis was processed with QuPath software.

Polyploidy assessment

To analyse polyploidy, liver sections were stained with Hoechst 33342, after which a dataset with nuclei size and circularity was extracted using QuPath. Then, by using R software, a dataset containing only hepatocyte nuclei was generated based on size (>30 µm) and circularity (>0.8). Nuclear ploidy was assessed automatically, by a specific macro developed with Image J software, as previously described (Gentric et al., 2015). Hepatocyte polyploidy is presented as the ratio between the number of polyploid cells and total hepatocytes.

Liver neutral lipid analysis

Hepatic lipids were extracted from liver samples as previously described elsewhere (Bligh EG, Dyer WJ, 1959). Briefly, 50 mg of liver were homogenized in 2:1 (v/v) methanol/EGTA (5mM) and lipids from 2mg of liver were extracted in a mix of methanol, chloroform and water (2.5:2.5:2, v/v/v) in the presence of internal standards (glyceryltrinonadecanoate, stigmasterol and cholesteryl heptadecanoate). Triglycerides, free cholesterol, and cholesterol esters were analyzed by gas chromatography on a Focus Thermo Electron system using a Zebron-1 Phenomenex fused-silica capillary column (5 m, 0.32 mm i.d., 0.50 µm film thickness). The oven temperature was programmed from 200 to 350°C at a rate of 5°C/min, and the carrier gas was hydrogen (0.5 bar). The injector and detector were at 315°C and 345°C, respectively.

Liver fatty acid analysis

Fatty acid methyl esters (FAME) molecular species were extracted from an equivalent of 1mg liver tissue in the presence of internal standards glyceryl triheptadecanoate (2 µg). The lipid extract was transmethylated with 1 ml BF3 in methanol (14% solution; Sigma) and 1 ml heptane for 60 min at 80°C and evaporated to dryness. The FAMEs were extracted with heptane/water (2:1). The organic phase was evaporated to dryness and dissolved in 50 µl ethyl acetate. A sample (1 µl) of total FAMEs was analyzed with gas-liquid chromatography (Clarus 600 Perkin

Elmer system, with Famewax RESTEK fused silica capillary columns, 30-m×0.32-mm i.d., 0.25-μm film thickness). Oven temperature was programmed to increase from 110°C to 220°C at a rate of 2°C/min, and the carrier gas was hydrogen (7.25 psi). Injector and detector temperatures were 225°C and 245°C, respectively.

Liver sphingomyelin and ceramide analysis

Lipids were extracted from the liver (1 mg) as described by Bligh and Dyer in dichloromethane/methanol (2% acetic acid)/water (2.5:2.5:2 v/v/v). Internal standards were added (Cer d18:1/15:0, 16 ng; SM d18:1/12:0, 16 ng). The solution was centrifuged at 1500 rpm for 3 min. The organic phase was collected and dried under azote, then dissolved in 50 μl MeOH. Sample solutions were analyzed with an Agilent 1290 UPLC system coupled to a G6460 triple quadripole spectrometer (Agilent Technologies). MassHunter software was used for data acquisition and analysis. A Kinetex HILIC column was used for LC separations. The column temperature was maintained at 40°C. The mobile phase A was Acetonitrile; and B was 10 mM ammonium formate in water at pH 3.2. The gradient was as follows: from 10% to 30% B in 10 min; 100% B from 10 to 12 min; and then back to 10% B at 13 min for 1 min to re-equilibrate prior to the next injection. The flow rate of the mobile phase was 0.3 ml/min, and the injection volume was 5 μl. An electrospray source was employed in positive ion mode. The collision gas was nitrogen. Needle voltage was set at +4000 V. Several scan modes were used. First, to obtain the naturally different masses of different species, we analyzed cell lipid extracts with a precursor ion scan at 184 m/z and 264 m/z for SM and Cer, respectively. The collision energy optimums for Cer, SM were 25 eV, 45 eV respectively. Then, the corresponding SRM transitions were used to quantify different phospholipid species for each class. Two 9 MRM acquisitions were necessary, due to important differences between phospholipid classes. Data were treated with QqQ Quantitative (vB.05.00) and Qualitative analysis software (vB.04.00).

Microarray based transcriptome profiling

Liver RNA extraction was performed as mentioned previously and checked for integrity using Bioanalyzer. Microarray experiment and data normalization were performed by the transcriptomic core facility at Cochin Institute. Briefly, gene expression profiling was carried out on 5 biological replicates per condition. After RNA quality validation with Bioanalyzer 2100, RNA was reversed transcribed following the manufacturer protocol (GeneChip® WT Plus Reagent Kit, Thermofisher). After fragmentation and biotin labelling, cDNA was hybridized to GeneChip® Clariom S Mouse (Thermofischer) and scanned using the GCS3000 7G. The images were analyzed with Expression Console software (Thermofischer). Raw data were normalized using the Robust Multichip Algorithm (RMA). Statistics and RMA normalization were performed using TAC4.0 software (Thermofisher).

Downstream analysis was done to identify differentially expressed (DE) genes based in comparison with control conditions. The DE genes were selected based on the corrected p-value for False Discovery Rate (FDR p-value < 0.05) and the fold change from OGT^{LKO} compared to controls (up-regulated genes: fold change ≥ 2, down-regulated genes: fold change ≤ -2). Venn diagram was performed using the interactive tool 'Venny 2.1.0' (Oliveros et al. 2007-2015). Up-regulated and down-regulated genes were annotated using Reactome gene set. Functional enrichment of specific pathways in the gene set was performed using Fisher's exact test and FDR correction. Pathways were considered significantly enriched at an FDR < 0.05. R statistical software v.3.6.2 and R packages were used for bioinformatic analysis and graph representation. Volcano plots were represented using the "Enhanced Volcano" package (Blighe et al. 2019). Heatmaps were represented using 'pheatmap' package (R. Kolde, 2019), where correlation clustering distance row was applied.

Primary hepatocyte isolation and culture

Four weeks old mice were anesthetized with a 10:1 ketamine-xylazine solution intra-peritoneal. Liver was perfused through the portal vein with Hank's balanced salt solution followed by collagenase perfusion. Cell viability was calculated by trypan blue exclusion test using a Malassez chamber and seeded in 6-well plates at a concentration of 500 000 cells per well. Cells were seeded in medium M199 5mM of glucose (Thermofisher, #11150059) supplemented with 100 µg/mL streptomycin, 100 units/mL of penicillin, L-glutamine (2 mM), 0.1% Bovine serum albumin, 2.5% Nu-serum (BD Bioscience, Cat#355104) and dexamethasone (100nM, Novo Nordisk). For reduced glutathione/oxidized glutathione (GSH/GSSG) assay, hepatocytes were seeded in 96-well plates at a concentration of 15 000 cells per well. Twenty-four hours after seeding, the GSH/GSSG ratio was measured using GSH/GSSG-Glo assay kit (Promega, Madison, WI) in accordance with the manufacturer's instructions. Experiments with Staurosporine were performed by seeding hepatocytes in 6 cm^2 dishes at a concentration of $1.5x10^6$ cells per dish. Twenty-four hours after seeding, cells were treated with 10µM of Staurosporine (Sigma, S4400) and harvested 0, 2, 4 and 8 hours after treatment for protein extraction. For Thapsigargin experiments, 24 hours after seeding, cells were treated with 0.3µM of Thapsigargin (Sigma, T9033) for 24 hours. Total level of lipid peroxidation was analyzed by flow cytometry-based Bodipy 581/591 assays (Molecular Probes), as recommended by the manufacturer. Forty-eight hours after seeding, cells were treated with 5 µM of BODIPY for 30 minutes at 37°C. Cells were then collected and washed with PBS. For each experiment, 20.000 events were acquired by flow cytometry using Novocyte Cytometer (Ozyme). Data were analysed using the Novoexpress Software. Total ROS levels were measured by using Cellrox Deep red Reagent (Thermofisher) at a final concentration of 2.5 µM and then incubated for 30 minutes at 37°C. Data were analysed using the Novoexpress Software. For ARE-luciferase activity, cells were transfected with a 3xARE-Luciferase reporter (Wang et al., 2006) and a β-

galactosidase plasmid using Lipofectamine 2000 and OptiMEM media. After overnight incubation, medium was changed to low glucose (5mM) for 24 hours. Luciferase assay was performed after cell lysis. β-galactosidase assays were performed for normalization of 3xARE-luciferase activity.

Second Harmonic Generation microscopy (SHG) for fibrosis quantification

SHG images were acquired with a multiphoton Leica DIVE microscope (Leica microsystems Gmbh, Wetzlar, Germany) coupled with a Coherent Discovery (Coherent Inc., Santa Clara, CA, USA) laser source. Five fields of view were acquired from paraffin embedded 7 µm-thick sections of liver. Two-photon-excited autofluorescence and SHG images were acquired through a Leica Microsystems HCX IRAPO 25x/0.95 water immersion objective by tuning the laser at 1040nm at constant power and photomultiplier tubes and hybrid detectors were used at constant 800V and 80% gain respectively allowing direct comparison of SHG intensity values. Circularly polarized laser pulse was sent to the microscope objective to excite isotropically the slice regardless of the orientation of fibrillar collagen. To quantify SHG, the microscope was calibrated using a non-fibrotic control liver section. SHG score was proceeded using a homemade ImageJ ((http://imagej.nih.gov/ij/)) routine, as described previously (Guilbert et al., 2010).

Statistical analysis

All statistical analysis were performed using Prism GraphPad Software Inc. The number of independent experiments performed and the statistical test used are indicated in each figure legend.

Results

Hepatocyte-specific OGT deletion triggers liver inflammation and moderate fibrosis at 4 weeks.

Four weeks after birth, fed blood glucose, body weight, liver and spleen weights were not found different in OGT^{LKO} compared to OGT^{LWT} mice (**Figure 1A**). OGT mRNA and protein levels (assessed by Western blot and immunostaining) were significantly reduced only in the liver of OGT^{LKO} mice, together with a parallel decrease in O-GlcNAcylated proteins (**Figures 1B, 1D** and **1E**) confirming recombination efficiency and tissue specificity. We also observed a significant decrease in OGA expression in the liver (**Figure 1C**). The activities of OGT and OGA are governed by multilayered feedback mechanisms that finely tune the overall levels of O-GlcNAcylation in the cell. Studies have established that alterations in OGA activity affect OGT activity and vice versa (Park et al., 2017). While the mechanism(s) used to modulate OGA protein levels in response to O-GlcNAc remain unknown, studies have suggested that OGA transcription is sensitive to changes in *O*-GlcNAc homeostasis and is potentially regulated by *O*-GlcNAc (Park et al., 2017). Physiological tests further analyses revealed decreased blood concentrations upon short-term fasting (5 hours) (**Figure S1A**), improved glucose (**Figure S1B**) and pyruvate tolerance (**Figure S1C**) in OGT^{LKO} compared to OGT^{LWT} mice, without, however, any modification in insulin sensitivity (**Figure S1D**). Decreased fasting blood glucose and increased pyruvate tolerance suggested decreased gluconeogenic capacity in OGT^{LKO} compared to OGT^{LWT} mice. To better understand the improvement in glucose homeostasis observed in OGT^{LKO} mice, we measured protein and the O-GlcNAcylation levels (Kuo et al., 2008) of the transcription factor Forkhead box protein o1 **(**Foxo1) (**Figure S1E**), that is known to stimulate the expression of gluconeogenic genes, including Glucose-6-phosphatase (*G6Pase*) and Phosphoenolpyruvate carboxykinase (*Pepck*) (**Figure S1F**). Of note, Foxo1 O-

GlcNAcylation levels were markedly decreased in liver of OGT^{LKO} compared to OGT^{LWT} mice (**Figure S1E**), as well as mRNA levels of its target genes (*G6Pase*, *Pepck*) (**Figure S1F**). Histological assessment by hematoxylin-eosin (HE), Sirius red or αSMA staining evidenced hepatic parenchymal alteration in OGT^{LKO} mice compared to OGT^{LWT}. In fact, OGT^{LKO} liver showed hepatocellular ballooning, and moderate fibrosis together with fibroblast activation (**Figure 1E**). In agreement, the expression of fibrosis markers (*Tgfβ*, *αSma*, *Col3a1* and *Col6a1*) was found significantly increased in livers of OGT^{LKO} mice compared to OGT^{LWT} (**Figure 1F**). In addition, positive staining for TUNEL, Krt7 (Cytokeratin7) and SOX9 in livers of 4 week-old OGT^{LKO} mice suggested emerging liver injury and apoptosis, ductular reaction and hepatic progenitor cell activation (**Figure 1E**). This observation was correlated with a significant increase in alanine aminotransferase (ALT) in OGT^{LKO} mice, while two other markers of liver injury (aspartate aminotransferase (AST) and lactate dehydrogenase (LDH)) were not found statistically different between the two groups of mice (**Figure 1G**). The expression of proliferation markers was also significantly induced in liver of OGT^{LKO} compared to OGT^{LWT} mice (*Ki67*, *CycA2*, *CycB1*, *CycD1)* (**Figure 1H**). To investigate the potential development of inflammation in the context of liver injury, we examined the expression of inflammatory markers. Significant induction of *Tnfα*, *Mcp1* and *Ccl5* was observed in the liver of OGT^{LKO} compared to OGT^{LWT} mice (**Figure 1I**). Analyses of serum pro-inflammatory cytokines and chemokines levels in 4 week-old mice also revealed a significant increase in C-X-C motif chemokine ligand 1 (Cxcl1) concentration (**Figure 1J**). Altogether, these results reveal that constitutive hepatic deletion of OGT in mice rapidly triggers early signs of liver injury, as illustrated by the onset of inflammation, apoptosis and moderate fibrosis at 4 weeks of age.

OGT^{LKO} mice exhibit necroptosis, extensive liver fibrosis and liver injury at 8 weeks.

To determine whether the emerging phenotype of liver injury observed in 4 week old OGT^{LKO} mice worsens with time, both male (**Figures 2 and Figure S2**) and female (**Figure S3**) OGT^{LKO} mice were studied 8 weeks after birth. Similar blood glucose concentrations and body weights were observed in 8 week-old male OGT^{LWT} and OGT^{LKO} mice (**Figure 2A**), while both liver and spleen weights were significantly increased in OGT^{LKO} compared to OGT^{LWT} mice, regarless of gender (**Figure 2A**). Interestingly, a dysmorphic liver with hepatic nodules together with splenomegaly was observed macroscopically at sacrifice in a large proportion of OGT^{LKO} mice (**Figure 2B)**. Macroscopic view of histological liver section of OGT^{LKO} mice from Sirius red staining showed a homogeneous distribution of these nodules, that were identified as regeneration nodules typical of chronically injured livers (**Figures 2B** and **2C**). Of note, clear signs of advanced hepatic fibrosis were observed in OGT^{LKO} liver sections, regardless of the presence of macroscopic regenerative nodules (**Figure S2D**). In agreement, mRNA levels of fibrosis markers (*Col3a1, Col6a1*) were significantly increased in both male and female OGT^{LKO} mice (**Figure 2D** and **Figure S3F**) and parallel Sirius red and αSMA staining showed fibroblast activation and advanced fibrosis in OGT^{LKO} livers (**Figure 2G** and **Figure S3D**). Surprisingly, analysis of OGT mRNA and protein levels revealed recovery of OGT expression in liver of OGT^{LKO} mice compared to OGT^{LWT} mice, despite a less pronounced effect in females than in males (**Figures 2E**, **2F** and **Figure S3C**). However, OGT immunolabelling showed OGT positive cells in OGT^{LKO} liver sections regardless of gender (**Figure 2G** and **Figure S3D**) , suggesting counter-selection against OGT deficient cells during liver regeneration (Baker et al., 2020). The emergence of TUNEL positive cells in OGT^{LKO} liver sections as well as Ki67 positive cells in hepatic tissue surrounding the regenerative nodules of OGT^{LKO} liver (**Figure 2G)** suggested an activation of both proliferation and apoptosis pathways. Accordingly, the expression of proliferation markers was significantly induced in liver of OGT^{LKO} compared to

OGT^{LWT} mice at both mRNA (*Ki67, CycA2, CycB1, CycD1)* and protein levels (Cyclin A, Cyclin D1, Proliferating cell nuclear antigen (PCNA) (**Figure S2B** and **2C**). While the expression of RIPK3 was unchanged in OGT^{LKO} livers, the expression of MLKL, another key protein of necroptosis, was significantly increased (**Figure 2H**). In agreement, OGT^{LKO} mice exhibited a significant increase in plasma ALT and LDH concentrations (**Figure 2I),** while the circulating levels of AST, another marker of liver injury was unchanged (**Figure S3E**). The expression of inflammatory markers (*Tnfα, Mcp1* and *Ccl5)* and plasma concentrations of cytokines (TNFα, IL-2, IL-6) were also increased in liver of OGT^{LKO} mice compared to the OGT^{LWT} control group (**Figures 2J** and **2K**). A similar phenotype comprising inflammation, fibrosis and liver injury was observed in 8 week-old OGT^{LKO} female mice (**Figure S3D** and **3H**). Therefore, either males and/or females were used in further experiments, as indicated in the figure legends. Finally, we next investigated whether OGT^{LKO} liver alterations were associated with early (4 weeks) or later (8 weeks) changes in cell identity following deletion of hepatic OGT (**Figure S2F**). A marked increase in mRNA levels of progenitor cells and cholangiocyte markers, *Krt7* and *Krt19,* was observed in livers of OGT^{LKO} compared to OGT^{LWT} mice both both ages, despite differences were more pronounced at 8 weeks (**Figure S2G**). Immunolabelling of HNF4α, SOX9 and Krt19 on liver sections confirmed a ductular reaction, mostly localized in the fibrosis septa in older OGT^{LKO} mice (**Figure S2H**). While total or direct bilirubin was not changed, a significant increase in serum alkaline phosphatase (ALP) was measured in 8 week-old OGT^{LKO} compared to OGT^{LWT} mice (**Figure S2E**). Taken together, our results suggest that OGT plays an important role in liver cell identity and that its deficiency leads to a rapid deterioration of liver homeostasis in OGT^{LKO} mice.

Hepatocyte OGT deletion leads to specific transcriptional changes in the liver from 4 and 8 week-old OGT^{LKO} mice.

To better characterize the early and late consequences of hepatic OGT deficiency, we performed a transcriptomic analysis on livers from 4 and 8 week old OGT^{LKO} and OGT^{LWT} mice. Volcano plots, that were generated by using a total of 22206 hepatic genes and by comparing OGT^{LKO} to OGT^{LWT} mice, demonstrated a shift in the expression levels of specific genes between the two time-points studied (4 and 8 weeks) (**Figures 3A** and **3B**). Venn diagram (fold change $\geq |2|$, false discovery rate (FDR) p-value < 0.05) indicated that 557 and 493 genes genes were differentially expressed (DE) at 4 and 8 weeks respectively, with 95 DE genes common to 4 and 8 week old mice (**Figure 3C, Table S3**). Several genes clusters were differentially regulated in OGT^{LKO} livers as compared to OGT^{LWT} at 4 and 8 weeks, as illustrated by the heatmap analysis (**Figure 3D**). Analysis of REACTOME pathways in the liver of 4 week-old mice showed a significant down-regulation in basic metabolic pathways such as lipid, amino acid and vitamin metabolism (**Figure 3E**). Interestingly, the glutathione metabolism pathway, an important detoxification pathway in the liver (Aquilano et al., 2014), was also significantly down-regulated at this stage (**Figure 3E**). In parallel, the expression of genes involved in immune signalling pathways and UDP-glucuronate formation, the latest known to be activated during antioxidant response in the liver (Kalthoff et al., 2010), were up-regulated at 4 weeks in OGT^{LKO} mice (**Figure 3F**). Surprisingly, analysis of DE genes at 8 weeks only reported up-regulated pathways. Up-regulation of genes involved in immune system activation suggested that the inflammation response was not resolved at 8 weeks. However, an up-regulation of pathways involved in liver injury and its resolution such as formation and degradation of extracellular matrix (ECM) was observed (**Figures 3F** and Figure **S4D**). Altogether, the results indicate specific changes in global mRNA expression occurring

between 4 and 8 weeks, indicating early and major molecular adaptations in the liver to cope with the loss of hepatic OGT.

OGT deficiency in hepatocytes leads to oxidative stress, ER stress and enhanced sensitivity to cell death.

Since the transcriptomic analysis revealed that a cluster of DE genes involved in the oxidative stress response was significantly up-regulated in OGT^{LKO} livers at 4 weeks (**Figure S4A**), we performed experiments in primary hepatocytes isolated from 4 week-old OGT^{LKO} mice. Interestingly, the GSH/GSSG ratio, a reliable indicator of oxidative stress, was significantly decreased in OGT^{LKO} compared to OGT^{LWT} hepatocytes, supporting enhanced hepatic oxidative stress response in 4 week-old OGT^{LKO} mice (**Figure 4A**). Because oxidative stress response involves binding of NRF2 (Nuclear factor erythroid-derived 2-related factor 2) on ARE (anti-oxidant response element) located on promoters of anti-oxidant response genes, we monitored NRF2 activity in OGT^{LKO} and OGT^{LWT} hepatocytes, by using an ARE luciferase reporter construct (Wang et al., 2006). ARE luciferase activity was increased by 7-fold in OGT^{LKO} hepatocytes compared to OGT^{LWT}, suggesting that the NRF2 antioxidant response was induced in the absence of OGT (**Figure 4B**). In agreement, an increase in p-p62 (autophagy related oxidative stress) (Cho et al., 2018; Manley et al., 2013), γH2AX (DNA damage) and CHOP (ER stress-derived apoptosis) was observed in hepatocytes from OGT deficient cells compared to OGT^{LWT} hepatocytes (**Figure 4C**). To further characterize oxidative stress in OGT^{LKO} hepatocytes, total ROS (reactive oxygen species) and total lipid peroxidation were assayed by CellROX and BODIPY assays. Both parameters were found significantly increased in OGT^{LKO} hepatocytes compared to OGT^{LWT} (**Figures 4D** and **4E**). Sensitivity of OGT^{LKO} hepatocytes to oxidative stress-dependent apoptosis was next evaluated over an 8 hour time-course in primary hepatocytes treated with staurosporine (StS) (Belmokhtar et al., 2001)

(**Figure 4F**). Higher levels of cleaved caspase-3, a marker of apoptosis, was observed in OGT deficient cells compared to OGT^{LWT} hepatocytes upon StS treatment, indicating enhanced sensitivity to StS-induced cell death (**Figure 4F**). Similarly, sensitivity to ER-stress induced apoptosis was also enhanced in OGT^{LKO} compared to OGT^{LWT} hepatocytes, as illustrated by significant higher levels of cleaved caspase-3 observed upon thapsigargin treatment (24 hours) (**Figure 4G**). Altogether, these data demonstrate that OGT deficiency promotes early oxidative and ER stress, leading to DNA damage and increased hepatocyte sensitivity to cell death.

OGT^{LKO} mice display extensive and prolonged hepatic fibrosis in response to early oxidative and ER stress

Aiming at better characterizing the phenotype of oxidative and ER stress in the OGT^{LKO} mice *in vivo,* we measured oxidative stress markers by qPCR in liver of 4 and 8 week-old OGT^{LKO} mice (**Figure 5**). These results confirmed a set of genes significantly induced at 4 weeks (*Nqo1*, *Gstm1*, *Gstm3*, *Gsta1*) but also at 8 weeks in liver of OGT^{LKO} mice, although to a lesser extent at 8 weeks than at 4 weeks (**Figures 5A** and **5B**). Similar changes were observed at the protein level for mediators of the oxidative/ER stress response (p-62, CHOP) and of DNA damage (γH2AX) (**Figures 5C** and **5D**). To better characterize the phenotype observed in OGT^{LKO} mice, we performed kinetic experiments and included an earlier time point (2 weeks) (**Figure S5**). Inflammation state occurred as early as 2 weeks after birth, with evidence of increased phosphorylation of c-Jun N-terminal kinase (JNK) in liver of 2 week-old OGT^{LKO} mice (**Figure S5A**). Of note, mRNA levels of oxidative stress (*Nqo1*, *Gstm1*, *Gstm3)* and ER stress markers (*Chop*) were significantly increased later on, between 4 and 8 weeks after birth (**Figures S5A** and **S5B**). However, staining with malondialdehyde (MDA), a commonly used marker for lipid peroxidation (Paradis et al., 1997), revealed positive staining on liver sections from 8 week-old OGT^{LKO} compared to OGT^{LWT} mice, confirming sustained hepatic stress at this stage of

development (**Figure 5E**). Finally, to better characterize the long term progression of hepatic damages in OGT^{LKO} mice, we followed mice up to 12 months, and sacrificed them at specific time points (8, 12 weeks and 12 months). While the expression of oxidative stress and inflammation markers was found increased in livers of OGT^{LKO} compared to OGT^{LWT} mice at 12 weeks, no difference between the two genotypes was observed when the mice were analysed at 12 months (**Figure S6B** and **6D).** In contrast, Sirius red staining revealed marked residual hepatic fibrosis in both 12 week-old and 12 month-old OGT^{LKO} mice (**Figure 5F**). In agreement, ALT serum levels were significantly increased in 12 week-old and 12 month-old OGT^{LKO} mice compared to controls **(Figure S6E**). Taken together, these data suggest that inflammation and oxidative stress are early triggering events of the the OGT^{LKO} phenotype peaking between 2 and 4 weeks, respectively. However, the rest of hepatic alterations of OGT^{LKO} mice (namely fibrosis and liver injury) persisted over time.

Low carbohydrate high fat (LCHF) diet prevents hepatic oxidative, ER stress, and DNA damage in OGT^{LKO} mice.

During the suckling period, pups receive a low carbohydrate high-fat diet that switches to a standard chow diet (SD) containing nearly 70% of carbohydrates at weaning. Because no oxidative stress was observed in livers of 2 week-old OGT^{LKO} mice, i.e. during the suckling period, we hypothesized that the elevated oxidative stress observed at 4 weeks could result from elevated carbohydrate content in the diet at weaning. Therefore, OGT^{LWT} and OGT^{LKO} mice were weaned and maintained for 5 weeks either on a standard diet (SD: 69% of carbohydrates, 4% of fat, 26% of proteins) or on a low carbohydrate diet compensated by lipid enhancement (LCHF: 21% of carbohydrates, 60% of fat, 19% of proteins) (**Figures 6** and **Figure S7A**). Induction of oxidative stress markers (*Gsta1*, *Gstm3*) in liver of OGT^{LKO} compared to OGT^{LWT} mice on standard diet (OGT^{LKO} SD *vs* OGT^{LWT} SD) was significantly reduced when OGT^{LKO}

mice were fed with LCHF (OGT^{LKO} LCHF) (**Figure 6A**). Interestingly, the expression of ER stress marker (CHOP) and DNA damage markers (γH2AX) was also reduced in liver of OGT^{LKO} LCHF mice when compared to OGT^{LKO} SD (**Figures 6B-D and Figure S7D**). OGT immunostaining revealed significant staining in liver sections from OGT^{LKO} mice regardless of the nutritional conditions (**Figure 6E**) in agreement with the re-expression observed on SD diet (**Figures 2E** and 2**F**). Histological analysis of liver ballooning (HE), inflammation (F4/80), ductular reaction (SOX9, Krt7), and fibrosis (Sirius red) showed no evidence of improvement upon LCHF conditions (**Figure 6E**). Quantification of fibrosis revealed similar hepatic fibrosis in OGT^{LKO} mice compared to OGT^{LWT} under either SD or LCHF diet (**Figure 6F**). In agreement, the expression of inflammatory markers (*Tnfα, Mcp1)* and fibrosis markers (*Col3a1* and *Col6a1*) was found similarly increased in livers of OGT^{LKO} mice compared to OGT^{LWT} in both nutritional challenges (**Figures 6H and 6G**). Nevertheless, a significant reduction in liver injury marker ALT was observed when OGT^{LKO} mice were weaned on a LCHF diet (**Figure 6I**) and a tendency in reduced circulating levels of inflammatory cytokine Cxcl1 (**Figure S7E**). Since specific lipids could contribute to oxidative stress and/or ER stress, the hepatic lipidomic profiling (including triglycerides, cholesterol, sphingolipids and fatty acids) of LCHF *vs* SD fed mice was performed (**Figure S9A**). Lipidomic analysis revealed that the majority of lipid species changes was due to the dietary change rather than to the genotype (clusters 1, 2, 4 and 5; **Figure S9A**). However, clusters 3 and 7 highlighted lipid signatures were respectively more (cluster 3) and less abundant (cluster 7) in OGT^{LKO} mice fed a LCHF diet compared to SD.

Taken together, these results suggest that while weaning OGT^{LKO} mice on a LCHF diet improved some parameters of liver damages (oxidative stress, ER stress and DNA damage), it failed to fully prevent hepatic alterations, such as ballooning, inflammation, ductular reaction and fibrosis.

Ketogenic diet prevents the hepatic alterations of OGT^{LKO} mice

Since the LCHF diet still contains 21% of carbohydrates, we hypothesized that further decreasing the carbohydrate content in the diet could improve the severe liver damage in OGT^{LKO} mice. Therefore, OGT^{LWT} and OGT^{LKO} mice were challenged at weaning with a ketogenic diet for 5 weeks (KD: 1% of carbohydrates, 94% of fat, 5% of protein) (**Figure S8A**). The significant induction of oxidative stress markers (*Gsta1*, *Gstm3*) in liver of OGT^{LKO} mice compared to OGT^{LWT} controls on standard diet (OGT^{LKO} SD *vs* OGT^{LWT} SD) was significantly reduced when OGT^{LKO} mice were weaned on KD (**Figure 7A**). Because oxidative stress has been shown to promote hyper-polyploidization of hepatocytes (Gentric et al., 2015), we quantified highly polyploid (≥8n) mononuclear hepatocytes relative to total hepatocytes in each group of mice. While the number of highly polyploid hepatocytes was significantly increased in liver of OGT^{LKO} SD mice when compared to OGT^{LWT} SD control (**Figure 7B**), no difference was observed between OGT^{LKO} and to OGT^{LWT} when fed on KD (**Figure 7B**), demonstrating that KD prevents the oxidative stress response upon hepatic OGT deficiency. The expression of ER stress (CHOP) and DNA damage (γH2AX) markers was also significantly reduced in the liver of OGT^{LKO} KD mice when compared to OGT^{LKO} SD (**Figures 7C-E** and **Figure S8D)**. OGT immunostaining revealed significant staining in liver sections from OGT^{LKO} mice regardless of the nutritional conditions (**Figure 7F**). Of note, in contrast to the histological observations made on a LCHF diet, liver ballooning (HE), inflammation (F4/80), ductular reaction (SOX9, Krt7), and fibrosis (Sirius red) were markedly improved in OGT^{LKO} mice upon KD conditions (**Figure 7F**). Quantification of fibrosis accordingly revealed a statistical decrease in hepatic fibrosis in OGT^{LKO} KD mice compared to OGT^{LKO} SD (**Figure 7G**). In agreement, the expression of fibrosis markers (*αSma*, *Col3a1* and *Col6a1*) was found similarly decreased in livers of OGT^{LKO} KD mice compared to OGT^{LKO} SD (**Figure 7H**). F4/80 staining show a marked reduction in liver section from OGT^{LKO} KD mice compared to OGT^{LKO} SD

(**Figure 7F**). Lastly, a significant difference was observed for liver injury marker ALT when OGT^{LKO} mice were weaned on a KD diet (**Figure 7J**). Interestingly, we also observed that specific hepatic lipid species previously associated with liver apoptosis and fibrosis (ceramides C24:0, C24:1) (Shmarakov et al., 2019; Pewzner-Jung et al., 2010) were no longer increased when OGT^{LKO} were weaned on KD (**Figure S9B**). Altogether, these results show that weaning on a KD fully prevented the phenotype of the OGT^{LKO} mice (oxidative stress, polyploidy, ER stress, inflammation, fibrosis and liver injury).

Discussion

In liver, O-GlcNAcylation has emerged as an important regulatory mechanism underlying normal liver physiology and metabolic disease (Yang and Qian, 2017). We previously reported that O-GlcNAcylation of two key transcription factors involved in glucose and lipid metabolism (i.e. ChREBP and Foxo1) significantly contributes to gluco-lipotoxicity in hepatocytes (Guinez et al., 2011; Kuo et al., 2008). However, the function of OGT in liver sensing appears rather complex since other studies reported that OGT is rather involved in the survival and death balance in hepatocytes, and also suggested that OGT acts as a critical modulator of hepatocytes homeostasis in the context of liver injury and/or chronic liver diseases (Zhang et al., 2019; Robarts et al., 2022).

To better understand the importance of O-GlcNAcylation signalling in hepatocytes, we generated mice with a liver-specific constitutive deletion of OGT (OGT^{LKO} mice) and examined their phenotype over a time course ranging from 2 weeks to 1 year upon different dietary challenges. Our specific goal was to address whether the lack of OGT could lead to oxidative stress and associated-liver injuries in a diet-dependent manner. We first evaluated glucose homeostasis parameters and observed a significant decrease in fasting blood glucose levels, as well as an improvement in both glucose and pyruvate tolerances when comparing OGT^{LKO} to

597 OGT^{LWT} mice at 4 weeks of age. In agreement, the expression of gluconeogenic genes was
598 significantly decreased in OGT^{LKO} liver. Interestingly, the O-GlcNAcylation of Foxo1, a
599 modification previously shown to regulate its transcriptional activity towards its target
600 gluconeogenic genes (Kuo et al., 2008; Housley et al., 2008) was significantly decreased in
601 liver of 4 week-old OGT^{LKO} compared to OGT^{LWT} mice. However, despite improvement in
602 metabolic homeostasis, clear signs of liver injury were already detectable at 4 weeks with a
603 significant increase in proliferation markers, elevated inflammation and moderate fibrosis,
604 suggesting a critical role for OGT in preventing hepatocyte insult. Indeed, experiments in
605 cultured OGT^{LKO} hepatocytes also confirmed oxidative stress, the later evidenced by a
606 significant decrease in the GSH/GSSG ratio, elevated total ROS production as well as lipid
607 peroxidation. Follow-up analysis of OGT^{LKO} mice demonstrated the development of
608 hepatomegaly, advanced fibrosis and cholestasis, features that persisted in one year-old
609 OGT^{LKO} mice, and that are usually seen in bile duct ligation models (Geerts et al., 2008).
610 Importantly, this severe hepatic phenotype was observed in both male and female OGT^{LKO}
611 mice, underlining the importance of using both genders in experimental research to better
612 understand how and why some diseases and conditions affect men and women differently.
613 Interestingly, while recent studies have revealed the existence of sexual dimorphisms in liver
614 diseases, in particular in Non-Alcoholic Fatty liver disease (NAFLD) and fibrosis onset
615 (Lefebvre and Staels 2021; Smati et al., 2022), we could not see any significant evidence when
616 comparing the phenotype of OGT^{LKO} males to OGT^{LKO} females.

617 The phenotype of liver OGT deficiency in hepatocytes also led to changes in cell identity
618 profile, probably favouring the differentiation of hepatoblasts to cholangiocytes, typical of the
619 ductular reaction produced in the initial steps of liver regeneration (Roskams et al., 2004).
620 Interestingly, higher number of highly polyploid hepatocytes was observed in liver of 8 week-
621 old OGT^{LKO} mice. While polyploidization can represent a gain of function by contributing to

622 tissue differentiation, we believe that the hyperpolyploidization observed was caused by
623 extensive cellular stress and can be considered here as a pathological lesion, as previously
624 suggested in other mouse models of hepatic oxidative stress (Gentric et al., 2015; Donne et al.,
625 2020).

626 A surprising observation was the partial recovery of OGT expression at 8 weeks of age
627 in livers of OGT^{LKO} mice. A similar phenomenon, which could be linked to counter-selection
628 (Baker, 2020) of OGT-expressing cells, has already been described for other liver specific gene
629 knock-out models (Yamaji et al., 2010; Zhang et al., 2010; Grindheim et al., 2019). Indeed,
630 hepatocytes deficient in OGT may encounter difficulties to survive in an oxidative and
631 inflammatory environment and enter a process of cell death, while hepatocytes escaping to the
632 recombination process will repopulate the liver with cells expressing OGT protein. In
633 agreement with this hypothesis, higher sensitivity to cell death-inducers was observed in
634 OGT^{LKO} compared to OGT^{LWT} hepatocytes. This increased susceptibility to cell death upon
635 defective O-GlcNAcylation is consistent with the significant necroptosis observed following
636 liver OGT deletion (Zang et al., 2019), and with enhanced necroptosis and apoptosis in liver of
637 OGT deficient mice after partial hepatectomy (Robarts et al., 2022). Several other mouse
638 models with liver-specific deficiency in proteins involved in DNA damage, such as Damage
639 specific DNA binding protein 1 (DDB1) (Yamaji et al., 2010), liver regeneration, such as Yes-
640 associated protein (YAP) (Zhang et al., 2010), or epigenetic modulation, such as Enhancer of
641 zeste homolog (EZH) 1/EZH2 (Grindheim et al., 2019), exhibited a phenomenon of cell
642 competition and recovery of expression of the targeted protein. However, the exact number of
643 cells that escapes recombination and the mechanisms involved in OGT recovery were not
644 clearly identified in the current study, and further analysis, including single cell RNAseq
645 analysis of OGT^{LKO} hepatocytes will be necessary to investigate these important questions. It
646 should be also mentioned that hepatic recovery of OGT was only partial in some of the groups

studied, as observed in livers of female OGT^{LKO} mice. The OGT recovery was not previously described in the published model of OGT liver knock-out mice (Zhang et al., 2019), but OGT expression in OGT^{LKO} mice was only documented at the age of 4 weeks in this study.

We believe that our study describes here a valuable and timely mouse model of spontaneous fibrosis that may facilitate therapeutic target identification for prevention and treatment of chronic liver disease. Indeed, induction of hepatic fibrosis in rodents requires the use of chemicals or specific diets, that while commonly used, often lack ease of use and appropriate relevance to human liver fibrosis (Yanguas et al., 2016). While efforts towards providing a better understanding of the mechanisms associated with fibrosis progression and/or regression are being made, no approved drugs are currently available for liver fibrosis *per se*. Interestingly, recent studies have highlighted that intrinsic metabolism of parenchymal cells, immune cells and/or hepatic stellate cells is important to sustain energetic needs of phenotypic changes in the context of fibrosis (Gilgenkrantz et al., 2021). In an attempt to decrease carbohydrate intake in OGT^{LKO} mice and to reduce oxidative stress associated with lack of OGT in liver, we first took the strategy to wean OGT^{LKO} mice on a LCHF diet in which the carbohydrate percentage is reduced by over 3-fold when compared to SD diet (69% of carbohydrates in SD *vs*. 21% in LCHF). This dietary switch while improving several parameters including oxidative stress and ER stress, did not correct the other liver alterations such as ballooning, macrophage infiltration, ductular reaction and fibrosis. However, when carbohydrate concentrations in the diet were further reduced and restricted to 1% in KD, full prevention of oxidative stress, hyperpolyploidy, inflammation and more importantly fibrosis and liver injury was observed. Of course, in the context of this nutritional switch, a protective role for lipids cannot be excluded, and in fact the combination of lowering carbohydrate intake and modulating specific lipid species could have been instrumental in the beneficial effects observed. Indeed, lipidomics analysis from LCHF and KD experiments revealed that OGT^{LKO}

mice exhibited high abundance of specific bioactive species including ceramides C24:0 and C24:1 under SD conditions, species which remain low upon KD conditions, suggesting that reduction in these ceramide moieties could contribute, at least in part, to the protective effect of KD on OGT^{LKO} mice. In addition, LCHF and KD also differ in their capacity to produce ketone bodies, especially β-hydroxybutyrate (**Figure S7C** and **Figure S8C**) a signalling metabolite with protective properties against oxidative stress (Rojas-Morales et al., 2020). While ketone body metabolism can induce oxidative stress, it was reported beneficial in the long term because it initiates an adaptive response characterized by the activation of the master regulators of cell-protective mechanism, including NRF2 (Kolb et al., 2021). This results in resolving oxidative stress, by the upregulation of anti-oxidative and anti-inflammatory activities, improved mitochondrial function, DNA repair and autophagy. In agreement, studies have hypothesized that activation of ketogenesis in the liver could potentially attenuate ROS-mediated NASH progression (Rojas-Morales et al., 2020).

Altogether, our study shows that hepatocyte-specific deletion of OGT leads to severe liver injury, confirming that O-GlcNAcylation and OGT are essential for hepatocytes homeostasis and survival. Our study also validates the OGT^{LKO} mouse model as a valuable model for the study of advanced liver fibrosis. Given that the severe fibrosis of OGT^{LKO} mice was fully prevented when mice were weaned on a very low carbohydrate high fat diet (i.e; ketogenic diet), our study underlines the potential interest of nutritional intervention as an anti-fibrogenic strategy.

Acknowledgements

The authors would like to thank Dr. Hélène Gilgenkrantz and Pr. Valérie Paradis (Centre de Recherche sur l'Inflammation (CRI), Université Paris Cité) for helpful discussions. We also would like to thank the Animal Facility from the Institut Cochin Inserm U1016, and in

particular Mathieu Benard for taking excellent care of the mice. We also thank the Institut Cochin platforms: the Genomic platform (GENOM'IC), the Cytometry and Immunobiology platform (CYBIO), the "Imagerie du vivant platform" (PIV) (Isabelle Lagoutte Franck Lager and Gilles Renault) and the Microscopy Platform (Thomas Guilbert) for fibrosis quantification. Lipidomic profiling was done in MetaToul-Lipidomique Core Facility (I2MC, Inserm 1297, Toulouse, France) from MetaToul (Toulouse metabolomics & fluxomics facilities, www.metatoul.fr) which is part of the French National Infrastructure for Metabolomics and Fluxomics MetaboHUB-ANR-11-INBS-0010.

Author contributions

P.O-P and L.P performed most the experiments with the help of F.B, M.R, I.C, M.M, N.P, J.M, P.P and M.C. R.O and M. F (HistIM Platform, Institut Cochin) performed liver sections and liver immunostaining. P.O-P analysed and interpreted the results from the microarray data. C.P, T.I, P.O-P, L.P prepared the figures and wrote the manuscript. J.G, C.D and SG provided scientific advice and critical reading of the manuscript. C.P and T.I conceptualized and supervised the project.

Declaration of interests

The authors declare no conflicts of interest.

References

Aquilano K, Baldelli S, Ciriolo MR. Glutathione: new roles in redox signaling for an old antioxidant. Front Pharmacol. 2014 Aug 26;5:196. doi: 10.3389/fphar.2014.00196. PMID: 25206336; PMCID: PMC4144092.

Baker NE. Emerging mechanisms of cell competition. Nat Rev Genet. 2020 Nov;21(11):683-697. doi: 10.1038/s41576-020-0262-8. Epub 2020 Aug 10. Erratum in: Nat Rev Genet. 2020 Aug 28;: PMID: 32778819; PMCID: PMC8205513.

Belmokhtar CA, Hillion J, Ségal-Bendirdjian E. Staurosporine induces apoptosis through both caspase-dependent and caspase-independent mechanisms. Oncogene. 2001 Jun 7;20(26):3354-62. doi: 10.1038/sj.onc.1204436. PMID: 11423986.

Chen PH, Chi JT, Boyce M. Functional crosstalk among oxidative stress and O-GlcNAc signaling pathways. Glycobiology. 2018 Aug 1;28(8):556-564. doi: 10.1093/glycob/cwy027. PMID: 29548027; PMCID: PMC6054262.

Cho CS, Park HW, Ho A, et al. Lipotoxicity induces hepatic protein inclusions through TANK binding kinase 1-mediated p62/sequestosome 1 phosphorylation. Hepatology. 2018 Oct;68(4):1331-1346. doi: 10.1002/hep.29742. Epub 2018 May 21. PMID: 29251796; PMCID: PMC6005718

de Carvalho Vidigal F, Guedes Cocate P, et al. The role of hyperglycemia in the induction of oxidative stress and inflammatory process. Nutr Hosp. 2012 Sep-Oct;27(5):1391-8. doi: 10.3305/nh.2012.27.5.5917. PMID: 23478683.

Dickinson S, Hancock DP, Petocz P, et al. High-glycemic index carbohydrate increases nuclear factor-kappaB activation in mononuclear cells of young, lean healthy subjects. Am J Clin Nutr. 2008 May;87(5):1188-93. doi: 10.1093/ajcn/87.5.1188. PMID: 18469238.

Donne R, Saroul-Aïnama M, Cordier P,et al.. Polyploidy in liver development, homeostasis

and disease. Nat Rev Gastroenterol Hepatol. 2020 Jul;17(7):391-405. doi: 10.1038/s41575-020-0284-x. Epub 2020 Apr 2. PMID: 32242122.

Du D, Shi YH, Le GW. Oxidative stress induced by high-glucose diet in liver of C57BL/6J mice and its underlying mechanism. Mol Biol Rep. 2010 Dec;37(8):3833-9. doi: 10.1007/s11033-010-0039-9. Epub 2010 Mar 9. PMID: 20217240.

Geerts AM, Vanheule E, Praet M, et al. Comparison of three research models of portal hypertension in mice: macroscopic, histological and portal pressure evaluation. Int J Exp Pathol. 2008 Aug;89(4):251-63. doi: 10.1111/j.1365-2613.2008.00597.x. PMID: 18715470; PMCID: PMC2525776.

Gentric G, Maillet V, Paradis V, et al.. Oxidative stress promotes pathologic polyploidization in nonalcoholic fatty liver disease. J Clin Invest. 2015 Mar 2;125(3):981-92. doi: 10.1172/JCI73957. Epub 2015 Jan 26. PMID: 25621497; PMCID: PMC4362240

Gilgenkrantz H, Mallat A, Moreau R, et al. Targeting cell-intrinsic metabolism for antifibrotic therapy. J Hepatol. 2021 Jun;74(6):1442-1454. doi: 10.1016/j.jhep.2021.02.012. Epub 2021 Feb 22. PMID: 33631228.

Grindheim JM, Nicetto D, Donahue G,et al. Polycomb Repressive Complex 2 Proteins EZH1 and EZH2 Regulate Timing of Postnatal Hepatocyte Maturation and Fibrosis by Repressing Genes With Euchromatic Promoters in Mice. Gastroenterology. 2019 May;156(6):1834-1848. doi: 10.1053/j.gastro.2019.01.041. Epub 2019 Jan 25. PMID: 30689973; PMCID: PMC6599454.

Guilbert T, Odin C, Le Grand Y, et al. A robust collagen scoring method for human liver fibrosis by second harmonic microscopy. Opt Express. 2010 Dec 6;18(25):25794-807. doi: 10.1364/OE.18.025794. PMID: 21164924.

Guinez C, Filhoulaud G, Rayah-Benhamed F, et al. C. O-GlcNAcylation increases ChREBP

764 protein content and transcriptional activity in the liver. Diabetes. 2011 May;60(5):1399-413.
765 doi: 10.2337/db10-0452. Epub 2011 Apr 6. PMID: 21471514; PMCID: PMC3292313.

766 Housley MP, Rodgers JT, Udeshi ND, et al. O-GlcNAc regulates FoxO activation in response
767 to glucose. J Biol Chem. 2008 Jun 13;283(24):16283-92. doi: 10.1074/jbc.M802240200. Epub
768 2008 Apr 17. PMID: 18420577; PMCID: PMC2423255

769 Kalthoff S, Ehmer U, Freiberg N, et al. Interaction between oxidative stress sensor Nrf2 and
770 xenobiotic-activated aryl hydrocarbon receptor in the regulation of the human phase II
771 detoxifying UDP-glucuronosyltransferase 1A10. J Biol Chem. 2010 Feb 26;285(9):5993-6002.
772 doi: 10.1074/jbc.M109.075770. Epub 2010 Jan 6. PMID: 20053997; PMCID: PMC2825393

773 Kolb H, Kempf K, Röhling M, et al. Ketone bodies: from enemy to friend and guardian angel.
774 BMC Med. 2021 Dec 9;19(1):313. doi: 10.1186/s12916-021-02185-0. PMID: 34879839;
775 PMCID: PMC8656040.

776 Kuo M, Zilberfarb V, Gangneux N, et al. O-glycosylation of FoxO1 increases its transcriptional
777 activity towards the glucose 6-phosphatase gene. FEBS Lett. 2008 Mar 5;582(5):829-34. doi:
778 10.1016/j.febslet.2008.02.010. Epub 2008 Feb 14. PMID: 18280254.

779 Lefebvre P, Staels B. Hepatic sexual dimorphism - implications for non-alcoholic fatty liver
780 disease. Nat Rev Endocrinol. 2021 Nov;17(11):662-670. doi: 10.1038/s41574-021-00538-6.
781 Epub 2021 Aug 20. PMID: 34417588.

782 Manley S, Williams JA, Ding WX. Role of p62/SQSTM1 in liver physiology and pathogenesis.
783 Exp Biol Med (Maywood). 2013 May;238(5):525-38. doi: 10.1177/1535370213489446.
784 PMID: 23856904; PMCID: PMC4096157.

785 Mohanty P, Hamouda W, Garg R, et al. Glucose challenge stimulates reactive oxygen species
786 (ROS) generation by leucocytes. J Clin Endocrinol Metab. 2000 Aug;85(8):2970-3. doi:
787 10.1210/jcem.85.8.6854. PMID: 10946914.

788 Nie H, Yi W. O-GlcNAcylation, a sweet link to the pathology of diseases. J Zhejiang Univ Sci
789 B. 2019 May;20(5):437-448. doi: 10.1631/jzus.B1900150. PMID: 31090269; PMCID:
790 PMC6568225.

791 Paradis V, Kollinger M, Fabre M, et al. In situ detection of lipid peroxidation by-products in
792 chronic liver diseases. Hepatology. 1997 Jul;26(1):135-42. doi:
793 10.1053/jhep.1997.v26.pm0009214462. PMID: 9214462

794 Park SK, Zhou X, Pendleton KE, et al. A Conserved Splicing Silencer Dynamically Regulates
795 O-GlcNAc Transferase Intron Retention and O-GlcNAc Homeostasis. Cell Rep. 2017 Aug
796 1;20(5):1088-1099. doi: 10.1016/j.celrep.2017.07.017. PMID: 28768194; PMCID:
797 PMC5588854.

798 Robarts DR, McGreal SR, Umbaugh DS, et al. Regulation of Liver Regeneration by Hepatocyte
799 O-GlcNAcylation in Mice. Cell Mol Gastroenterol Hepatol. 2022;13(5):1510-1529. doi:
800 10.1016/j.jcmgh.2022.01.014. Epub 2022 Jan 28. PMID: 35093590; PMCID: PMC9043307

801 Rojas-Morales P, Pedraza-Chaverri J, Tapia E. Ketone bodies, stress response, and redox
802 homeostasis. Redox Biol. 2020 Jan;29:101395. doi: 10.1016/j.redox.2019.101395. Epub 2019
803 Nov 28. PMID: 31926621; PMCID: PMC6911969.

804 Roskams TA, Theise ND, Balabaud C, et al. Nomenclature of the finer branches of the biliary
805 tree: canals, ductules, and ductular reactions in human livers. Hepatology. 2004
806 Jun;39(6):1739-45. doi: 10.1002/hep.20130. PMID: 15185318.

807 Shafi R, Iyer SP, Ellies LG, et al. The O GlcNAc transferase gene resides on the X chromosome
808 and is essential for embryonic stem cell viability and mouse ontogeny. Proc Natl Acad Sci U S
809 A. 2000 May 23;97(11):5735-9. doi: 10.1073/pnas.100471497. PMID: 10801981; PMCID:
810 PMC18502.

811 Shmarakov IO, Jiang H, Liu J, et al. Hepatic stellate cell activation: A source for bioactive

lipids. Biochim Biophys Acta Mol Cell Biol Lipids. 2019 May;1864(5):629-642. doi: 10.1016/j.bbalip.2019.02.004. Epub 2019 Feb 5. PMID: 30735856; PMCID: PMC6414233.

Smati S, Polizzi A, Fougerat A, et al. Integrative study of diet-induced mouse models of NAFLD identifies PPARα as a sexually dimorphic drug target. Gut. 2022 Apr;71(4):807-821. doi: 10.1136/gutjnl-2020-323323. Epub 2021 Apr 26. PMID: 33903148

Toda G, Ikeda Y, Kako M, et al. Mechanism of elevation of serum alkaline phosphatase activity in biliary obstruction: an experimental study. Clin Chim Acta. 1980 Oct 23;107(1-2):85-96. doi: 10.1016/0009-8981(80)90417-9. PMID: 7428180.Wang XJ, Hayes JD, Wolf CR. Generation of a stable antioxidant response element-driven reporter gene cell line and its use to show redox-dependent activation of nrf2 by cancer hemotherapeutic agents. (2006) Cancer Res. 15;66(22):10983-94. doi: 10.1158/0008-5472.CAN-06-2298.

Wang XJ, Hayes JD, Wolf CR. Generation of a stable antioxidant response element-driven reporter gene cell line and its use to show redox-dependent activation of nrf2 by cancer chemotherapeutic agents. Cancer Res. 2006 Nov 15;66(22):10983-94. doi: 10.1158/0008-5472.CAN-06-2298. PMID: 17108137.

Yanguas SC, Cogliati B, Willebrords J, et al. Experimental models of liver fibrosis. Arch Toxicol. 2016 May;90(5):1025-1048. doi: 10.1007/s00204-015-1543-4. Epub 2015 Jun 6. PMID: 26047667; PMCID: PMC4705434.

Yamaji S, Zhang M, Zhang J, et al. Hepatocyte-specific deletion of DDB1 induces liver regeneration and tumorigenesis. Proc Natl Acad Sci U S A. 2010 Dec 21;107(51):22237-42. doi: 10.1073/pnas.1015793108. Epub 2010 Dec 6. PMID: 21135245; PMCID: PMC3009836.

Yang X, Qian K. Protein O-GlcNAcylation: emerging mechanisms and functions. Nat Rev Mol Cell Biol. 2017 Jul;18(7):452-465. doi: 10.1038/nrm.2017.22. Epub 2017 May 10. PMID: 28488703; PMCID: PMC5667541.

Zhang B, Li MD, Yin R, et al. O-GlcNAc transferase suppresses necroptosis and liver fibrosis. JCI Insight. 2019 Nov 1;4(21):e127709. doi: 10.1172/jci.insight.127709. PMID: 31672932; PMCID: PMC6948774.

Zhang N, Bai H, David KK, et al. The Merlin/NF2 tumor suppressor functions through the YAP oncoprotein to regulate tissue homeostasis in mammals. Dev Cell. 2010 Jul 20;19(1):27-38. doi: 10.1016/j.devcel.2010.06.015. PMID: 20643348; PMCID: PMC2925178.

Figures Legends

Figure 1. Hepatocyte-specific OGT deletion leads to liver inflammation and moderate liver injury at 4 weeks.

Male liver-specific *Ogt* knockout (OGT^{LKO}) and control floxed littermates (OGT^{LWT}) mice were studied 4 weeks after birth in the fed state. **A.** Fed blood glucose (mmol/L), body (g), liver and spleen weights are shown. Liver and spleen weights are represented as percentage of body weight. **B**. Relative *Ogt* expression normalized to TBP (TATA-box binding protein). **C**. Relative *Oga* expression normalized to TBP. **D**. Western blot analysis of OGT and O-GlcNAcylation levels in liver, muscle, white adipose (WAT), brown adipose (BAT) tissue of OGT^{LWT} and OGT^{LKO} mice. Tubulin was used as loading control. One representative sample is presented per condition. **E**. Liver sections stained with hematoxylin-eosin (HE), Sirius Red, αSMA, Krt7, OGT, SOX9 and TUNEL. Scale bars = 100 μm. **F**. Relative expression levels of fibrosis markers normalized to TBP. **G**. Serum levels of alanine aminotransferase (ALT), aspartate aminotransferase (AST) and lactate dehydrogenase (LDH). **H**. Relative expression levels of proliferation markers normalized to TBP. **I.** Relative expression levels of inflammatory markers normalized to TBP. **J**. Serum levels of Cxcl1. Data are shown as Mean ± SEM of 5-10 individual male mice. *P < 0.05; **P < 0.01; ***P < 0.001 by unpaired Student t-test (Mann-Whitney).

Figure 2. OGT^{LKO} mice exhibit liver extensive fibrosis at 8 weeks.

Male liver-specific *Ogt* knockout (OGT^{LKO}) and control floxed littermates (OGT^{LWT}) mice were studied 8 weeks after birth in the fed state. **A**. Fed blood glucose (mmol/L), body weight (g), liver and spleen weights are shown. Liver and spleen weights are represented as percentage of body weight. **B**. Macroscopic view of spleen and liver from OGT^{LWT} (left) and OGT^{LKO} (right)

mice. **C**. Macroscopic view of histological liver section stained with Sirius red. **D**. Relative expression levels of fibrosis markers normalized to TBP. **E**. Expression levels of OGT normalized to TBP. **F**. Western blots of OGT content and O-GlcNAcylation levels in liver of OGT^{LWT} and OGT^{LKO} mice at 8 weeks. Three representative samples are shown. Actin was used for normalization. **G**. Liver sections stained with hematoxylin-eosin (HE), Sirius red, αSMA, OGT, Ki67 and TUNEL. Scale bars = 100 μm. **H.** Western blot analysis of necroptosis proteins (MLKL and RIPK3). Six representative samples are shown. Tubulin was used for normalization and quantification. **I**. Serum levels of alanine aminotransferase (ALT) and lactate dehydrogenase (LDH). **J**. Relative expression levels of inflammatory markers normalized to TBP. **K**. Serum levels of inflammatory cytokines. Data are shown as Mean ± SEM of 13-15 male mice per condition. *P < 0.05; **P < 0.01; ***P < 0.001 by unpaired Student t-test (Mann-Whitney).

Figure 3. Microarray analysis in liver reveals specific transcriptional changes at 4 and 8 weeks in OGT^{LKO} mice. Results were generated using microarray data from 5 replicates per condition. **A**-**B**. Volcano plot representing differential gene expression of 22206 genes comparing livers from OGT^{LKO} and OGT^{LWT} mice 4 (**A**) and 8 (**B**) weeks after birth. Log_2FC (fold change) is represented in the X-axis and $log_{10}FDR$ (False Discovery Rate) p-value in the Y-axis. Fold change ≥ |2| and FDR p-value < 0.05 were taken as cut-off parameters for selection of differentially expressed (DE) genes, represented in red. **C**. Venn diagram of DE genes in the liver of 4 and 8 week-old mice. **D**. Hierarchical clustering showing differential expression of genes in liver of OGT^{LKO} mice compared to OGT^{LWT}. **E-F**. Top REACTOME pathways significantly up- or down-regulated using the DE genes between male OGT^{LKO} and OGT^{LWT} mice at 4 (**E**) or 8 (**F**) weeks.

Figure 4. Hepatic OGT deficiency leads to oxidative stress, ER stress, DNA damage and enhanced sensitivity to cell death.

Experiments were performed in primary cultured hepatocytes from 4 week-old male and female mice. **A**. Ratio of reduced to oxidized glutathione (GSH/GSSG). **B**. NRF2 activity measured upon transfection with a plasmid containing a 3xARE-luciferase NRF2 reporter gene. **C.** Western blot analysis of OGT, markers of oxidative stress, ER stress and DNA damage markers. Two representative samples are shown. **D**. Total ROS levels measured by CellRox (Ozyme). **E**. Lipid peroxidation analyzed by flow cytometry-based Bodipy 581/591 assays (Molecular Probes). **F**. Western blot analysis of OGT and cleaved caspase-3 after 8h of staurosporine (StS) treatment. Actin was used as a loading control and quantification for 8 hours post StS treatment is shown. **G**. Western blot analysis of OGT and cleaved caspase-3 after 24h of Thapsigargin treatment. Actin was used as a loading control and quantification for cleaved caspase 3 is shown. Data are shown as Mean ± SEM of two to five independent cultures done in triplicate. *P < 0.05; ***P < 0.001; ****P < 0.0005 by unpaired Student t-test (Mann-Whitney).

Figure 5. Oxidative stress, ER stress, lipid peroxidation and DNA damage in liver of 4 and 8 weeks old OGT^{LKO} mice.

Male liver-specific *Ogt* knockout (OGT^{LKO}) and control floxed littermates (OGT^{LWT}) mice were studied 4 and 8 weeks after birth in the fed state. **A**. Relative expression levels of oxidative stress markers normalized to TBP. **B**. Relative expression of *Chop* normalized to TBP. **C.** Western blots showing protein content in whole liver lysates of markers of oxidative stress (p-p62), ER stress (CHOP) and DNA damage (γH2A.X) normalized to Actin. Cropped membranes are indicated with discontinued lines. **D**. Quantification of p-p62, CHOP and γH2A.X is shown. **E**. Malondialdehyde (MDA) staining, in liver sections from 4 and 8 week-old OGT^{LWT} and

927 OGT^{LKO} mice. Scale bars = 100 μm. **F**. Liver sections from OGT^{LWT} and OGT^{LKO} mice at 12
928 weeks and 12 months of age stained with Sirius red. Scale bars = 100 μm. Data are shown as
929 Mean ± SEM of 8-10 mice at 4 weeks, 13-15 mice at 8 weeks, 18-20 mice at 12 weeks and 18-
930 20 mice at 1 year. *P < 0.05; **P < 0.01; ***P < 0.001 by unpaired Student t-test (Mann-
931 Whitney).
932
933 **Figure 6. Low carbohydrate high fat (LCHF) diet improves oxidative stress, ER stress**
934 **and DNA damage but not fibrosis in OGT^{LKO} mice.**
935 Liver-specific *Ogt* knockout (OGT^{LKO}) and control floxed littermates (OGT^{LWT}) mice (males
936 and females) were weaned (at 3 weeks of age) on a low carbohydrate high fat (LCHF) diet and
937 sacrificed 5 weeks later in the fed state. **A**. Relative expression levels of oxidative stress markers
938 normalized to TBP. **B**. Western blot analysis of CHOP protein content in liver of OGT^{LWT} and
939 OGT^{LKO} mice either on SD or LCHF diet. Four representative samples are shown. **C.** Western
940 blot analysis of γH2AX protein content in liver of OGT^{LWT} and OGT^{LKO} mice either on SD or
941 LCHF diet. Three representative samples are shown. **D**. Quantification of CHOP and γH2AX
942 is shown. Actin was used as a loading control. **E**. Liver sections stained with hematoxylin-
943 eosin (HE), F4/80, Sox9, Krt7, Sirius red and OGT. Scale bars = 50 μm. **F**. Quantification of
944 fibrosis by second Harmonic Generation microscopy (SHG). **G**. Relative expression levels of
945 fibrosis markers normalized to TBP. **H**. Relative expression levels of inflammatory markers
946 normalized to TBP. **I**. Serum levels of alanine aminotransferase (ALT) and alkaline
947 phosphatase (ALP). Data are shown as Mean ± SEM of 4-13 mice (males and females). *P <
948 0.05; **P < 0.01; ***P < 0.001; ****P < 0.0005 by unpaired Student t-test (Mann-Whitney).
949
950 **Figure 7. Ketogenic diet (KD) improves oxidative stress, ER stress, DNA damage, hepatic**
951 **fibrosis and liver injury in OGT^{LKO} mice**

Liver-specific *Ogt* knockout (OGT^{LKO}) and control floxed littermates (OGT^{LWT}) mice (males and females) were weaned (at 3 weeks of age) on ketogenic diet (KD) diet and sacrificed 5 weeks later in the fed state. **A**. Relative expression levels of oxidative stress markers normalized to TBP. **B**. The proportion of highly polyploid (≥8n) mononuclear hepatocytes relative to total hepatocytes was quantified in each group. Blue: plasma membrane labeling (KL1). Red: nuclear labelling (Hoechst) (scale bar=100 μm). **C**. Western blot analysis of CHOP protein content in livers of OGT^{LWT} and OGT^{LKO} mice. Three to four representative samples are shown. **D.** Western blot analysis of γH2AX protein content in livers of OGT^{LWT} and OGT^{LKO} mice. Three to four representative samples are shown. **E**. Quantification of CHOP and γHA2X are shown. Actin was used as a loading control. **F.** Liver sections stained with hematoxylin-eosin (HE), F4/80, Sox9, Krt7, Sirius red and OGT. Scale bars = 100 μm. **G**. Quantification of fibrosis by second Harmonic Generation microscopy (SHG). **H**. Relative expression levels of fibrotic markers normalized to TBP. **I**. Relative expression levels of inflammatory markers normalized to TBP. **J**. Serum levels of alanine aminotransferase (ALT) and alkaline phosphatase (ALP). Data are shown as Mean ± SEM of 4-8 mice (males and females). *P < 0.05; **P < 0.01; ***P < 0.001; ****P< 0.0005 by unpaired Student t-test (Mann-Whitney).

Figure

Click here to access/download;Figure;OGT Figures Rev 23 06 v3.pptx

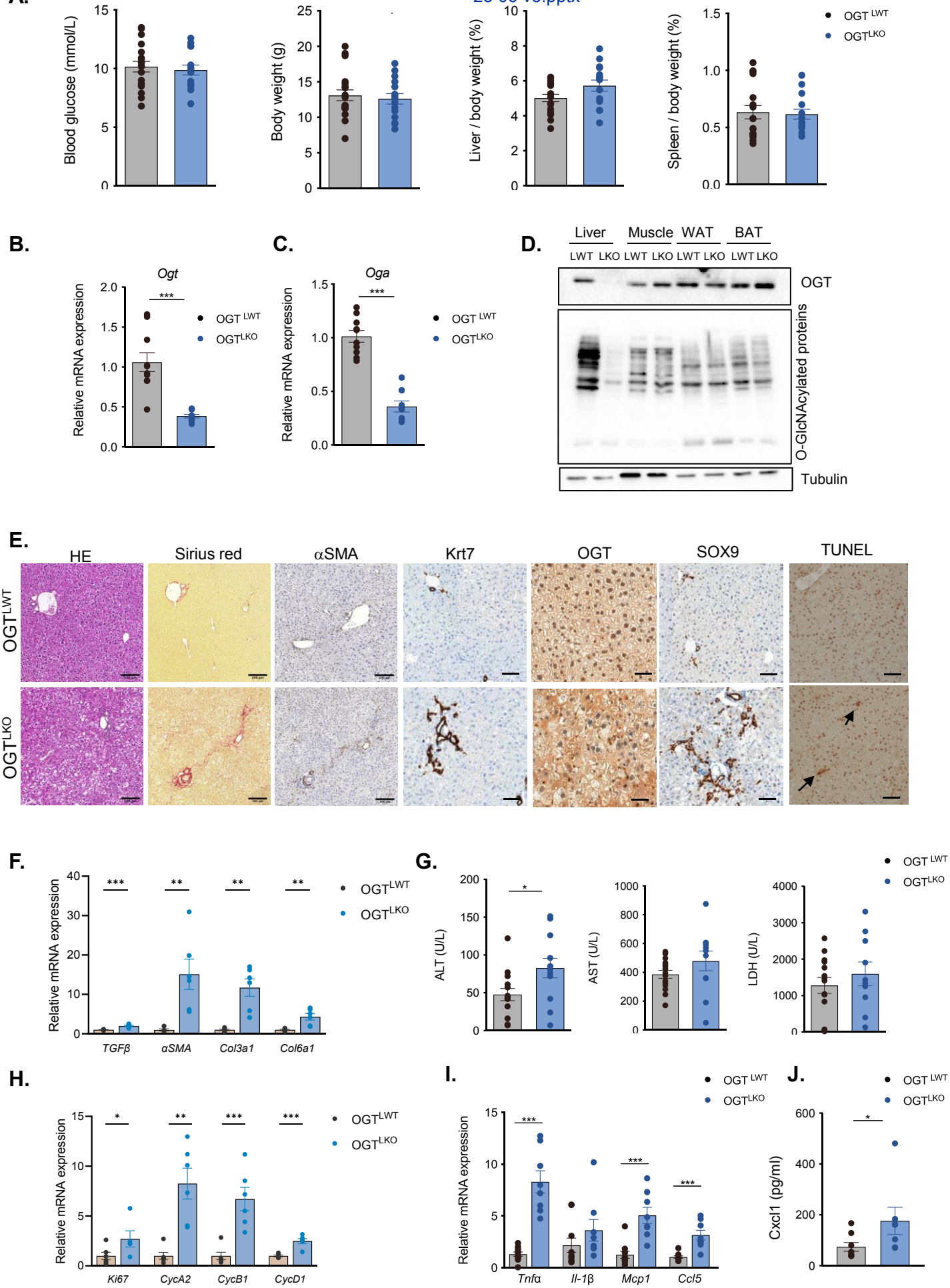

Figure 1

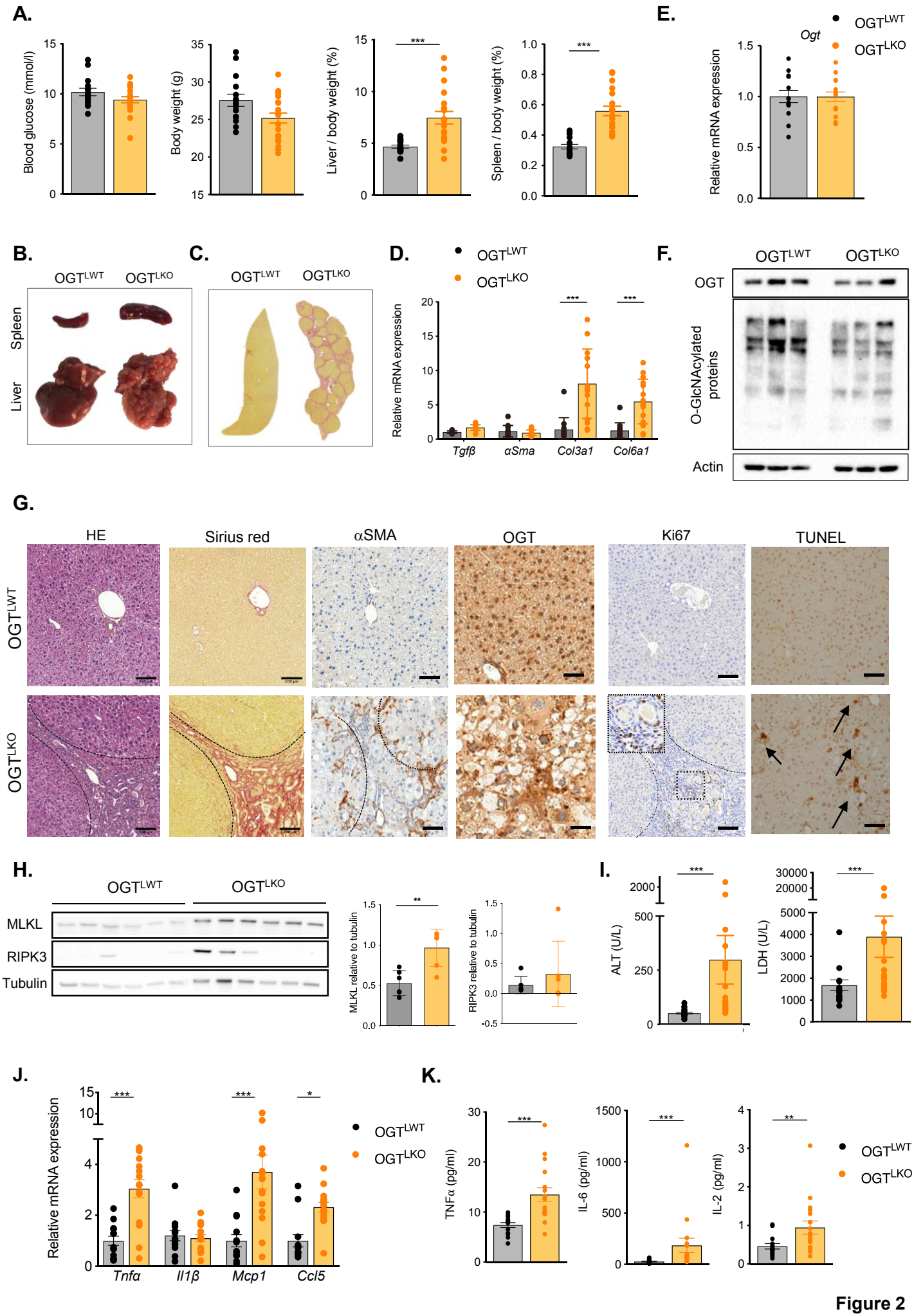
A.
Blood glucose (mmol/l)
Body weight (g)
Liver / body weight (%)
Spleen / body weight (%)
***
B.
OGTLWT
OGTLKO
Spleen
Liver
C.
D.
Relative mRNA expression
Tgfβ
αSma
Col3a1
Col6a1
E.
Ogt
Relative mRNA expression
F.
OGT
O-GlcNAcylated proteins
Actin
G.
HE
Sirius red
αSMA
OGT
Ki67
TUNEL
H.
MLKL
RIPK3
Tubulin
MLKL relative to tubulin
RIPK3 relative to tubulin
I.
ALT (U/L)
LDH (U/L)
J.
Tnfα
Il1β
Mcp1
Ccl5
K.
TNFα (pg/ml)
IL-6 (pg/ml)
IL-2 (pg/ml)

Figure 2

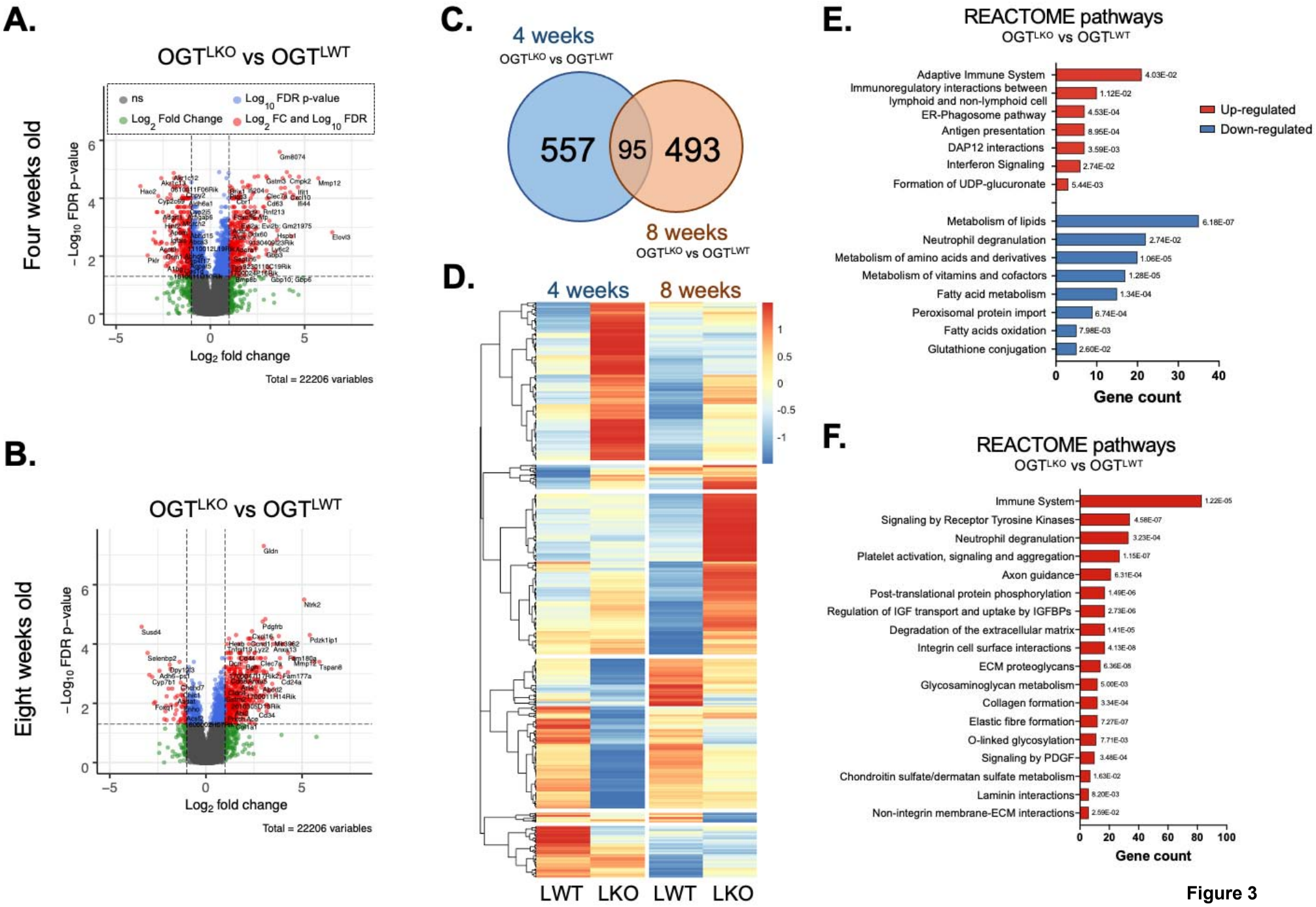
A.
OGTLKO vs OGTLWT
Four weeks old
ns
Log10 FDR p-value
Log2 Fold Change
Log2 FC and Log10 FDR
−Log10 FDR p−value
Log2 fold change
Total = 22206 variables
B.
OGTLKO vs OGTLWT
Eight weeks old
−Log10 FDR p−value
Log2 fold change
Total = 22206 variables
C.
4 weeks
OGTLKO vs OGTLWT
557
95
493
8 weeks
OGTLKO vs OGTLWT
D.
4 weeks
8 weeks
LWT
LKO
LWT
LKO
E.
REACTOME pathways
OGTLKO vs OGTLWT
Adaptive Immune System 4.03E-02
Immunoregulatory interactions between lymphoid and non-lymphoid cell 1.12E-02
ER-Phagosome pathway 4.53E-04
Antigen presentation 8.95E-04
DAP12 interactions 3.59E-03
Interferon Signaling 2.74E-02
Formation of UDP-glucuronate 5.44E-03
Metabolism of lipids 6.18E-07
Neutrophil degranulation 2.74E-02
Metabolism of amino acids and derivatives 1.06E-05
Metabolism of vitamins and cofactors 1.28E-05
Fatty acid metabolism 1.34E-04
Peroxisomal protein import 6.74E-04
Fatty acids oxidation 7.98E-03
Glutathione conjugation 2.60E-02
Up-regulated
Down-regulated
Gene count
F.
REACTOME pathways
OGTLKO vs OGTLWT
Immune System 1.22E-05
Signaling by Receptor Tyrosine Kinases 4.58E-07
Neutrophil degranulation 3.23E-04
Platelet activation, signaling and aggregation 1.15E-07
Axon guidance 6.31E-04
Post-translational protein phosphorylation 1.49E-06
Regulation of IGF transport and uptake by IGFBPs 2.73E-06
Degradation of the extracellular matrix 1.41E-05
Integrin cell surface interactions 4.13E-08
ECM proteoglycans 6.36E-08
Glycosaminoglycan metabolism 5.00E-03
Collagen formation 3.34E-04
Elastic fibre formation 7.27E-07
O-linked glycosylation 7.71E-03
Signaling by PDGF 3.48E-04
Chondroitin sulfate/dermatan sulfate metabolism 1.63E-02
Laminin interactions 8.20E-03
Non-integrin membrane-ECM interactions 2.59E-02
Gene count

Figure 3

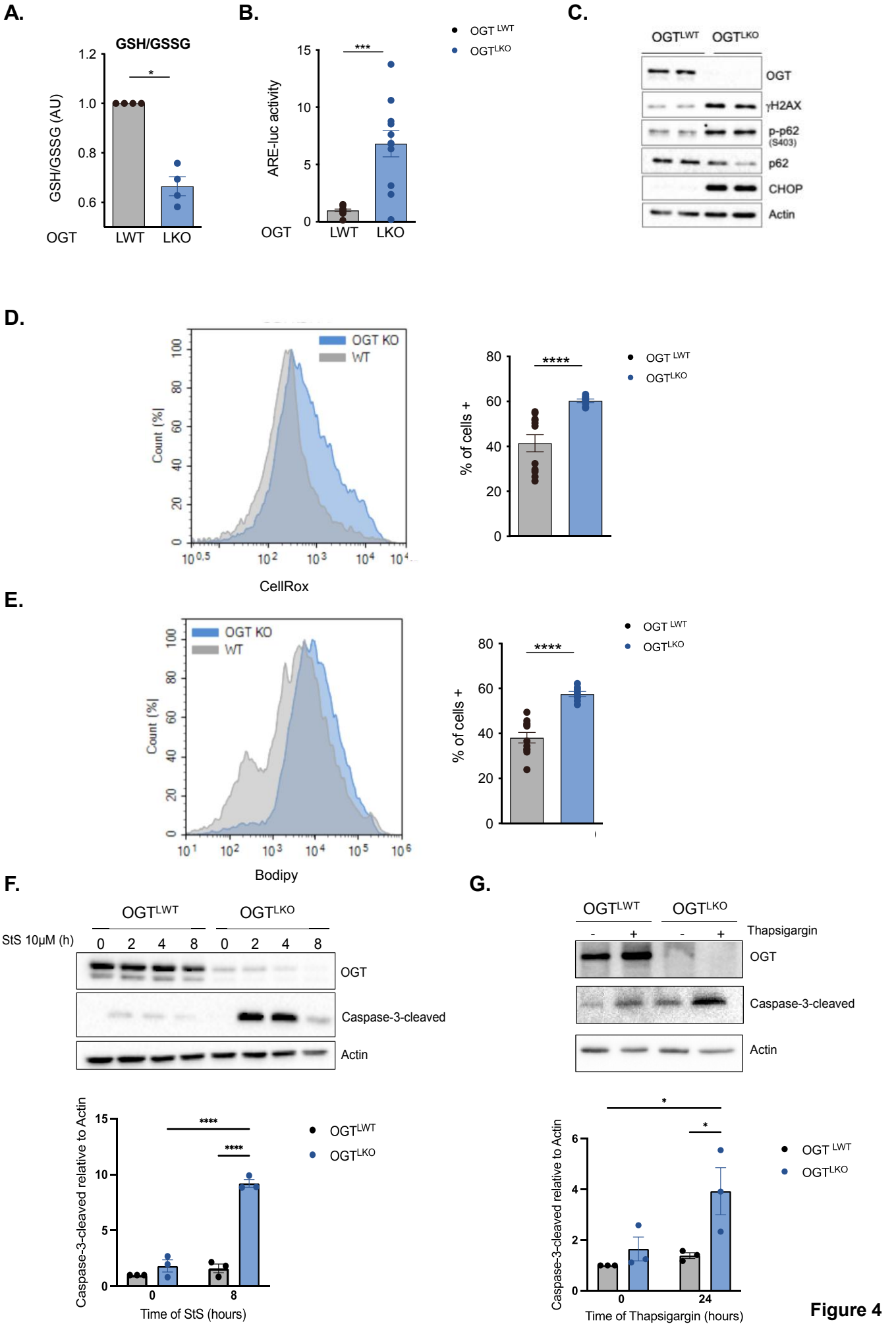
A.
GSH/GSSG
GSH/GSSG (AU)
OGT
LWT
LKO
B.
ARE-luc activity
OGT LWT
OGTLKO
C.
OGTLWT
OGTLKO
OGT
γH2AX
p-p62 (S403)
p62
CHOP
Actin
D.
OGT KO
WT
Count [%]
CellRox
% of cells +
E.
Bodipy
F.
StS 10μM (h)
Caspase-3-cleaved
Caspase-3-cleaved relative to Actin
Time of StS (hours)
G.
Thapsigargin
Time of Thapsigargin (hours)

Figure 4

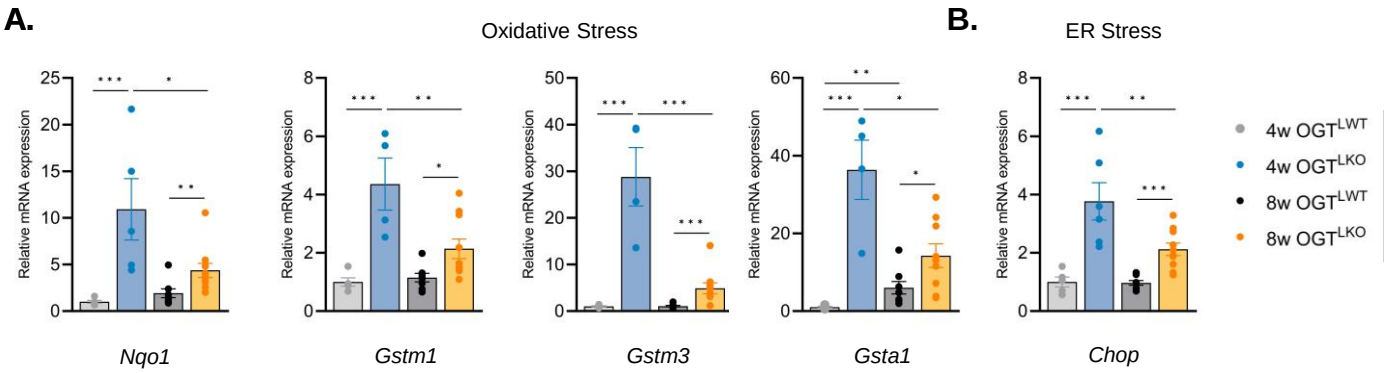
A.
Oxidative Stress
B.
ER Stress
Relative mRNA expression
Nqo1
Gstm1
Gstm3
Gsta1
Chop
4w OGTLWT
4w OGTLKO
8w OGTLWT
8w OGTLKO

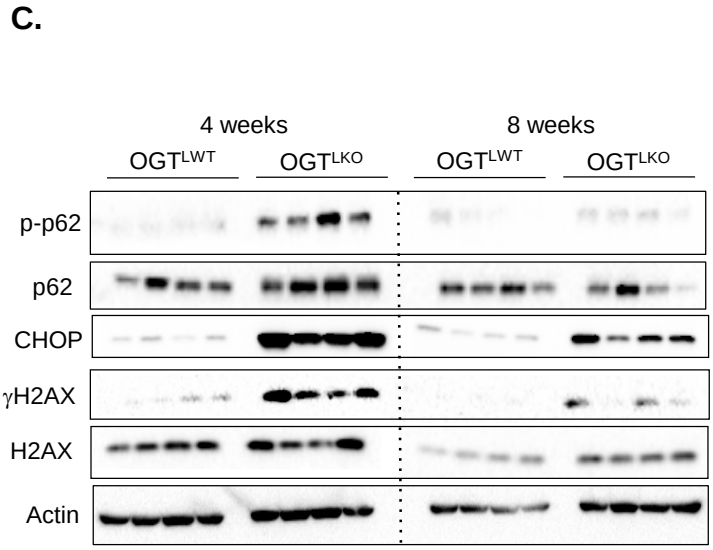
C.
4 weeks
8 weeks
OGTLWT
OGTLKO
OGTLWT
OGTLKO
p-p62
p62
CHOP
γH2AX
H2AX
Actin

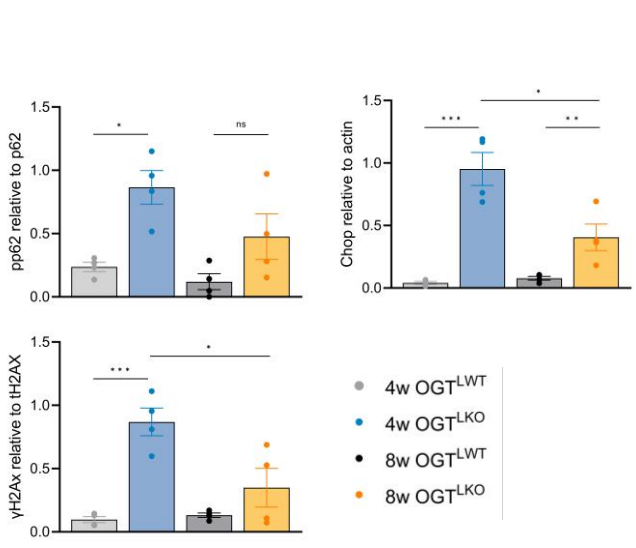
D.
pp62 relative to p62
Chop relative to actin
γH2Ax relative to tH2AX
4w OGTLWT
4w OGTLKO
8w OGTLWT
8w OGTLKO

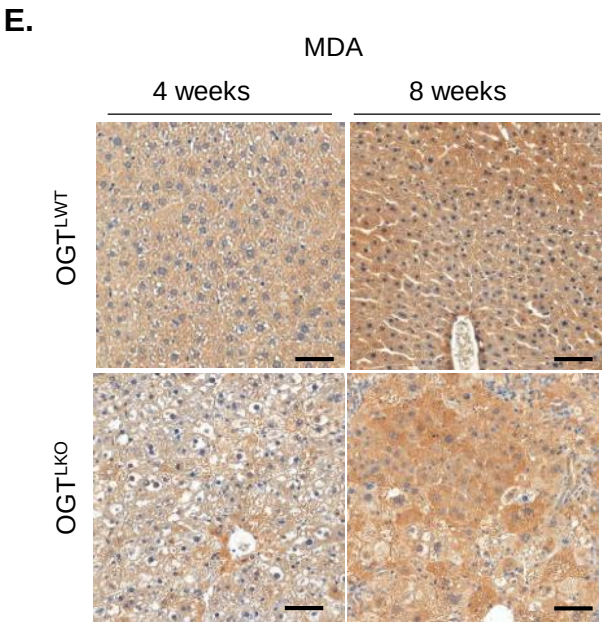
E.
MDA
4 weeks
8 weeks
OGTLWT
OGTLKO

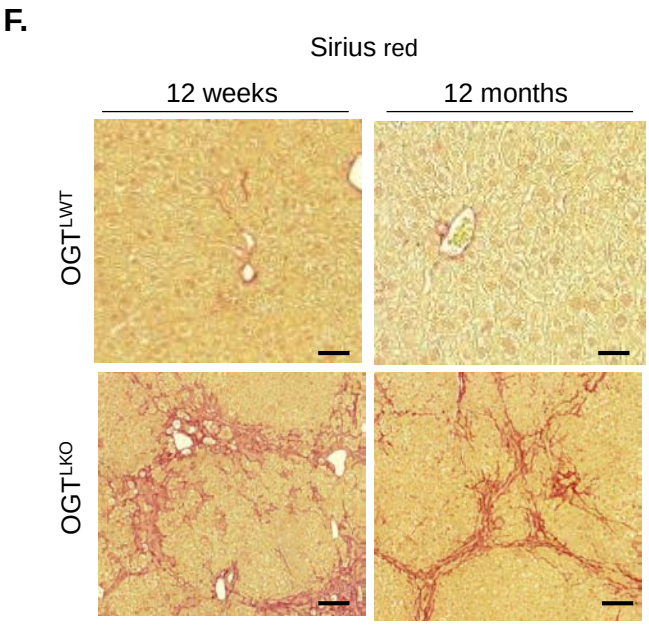
F.
Sirius red
12 weeks
12 months
OGTLWT
OGTLKO

Figure 5

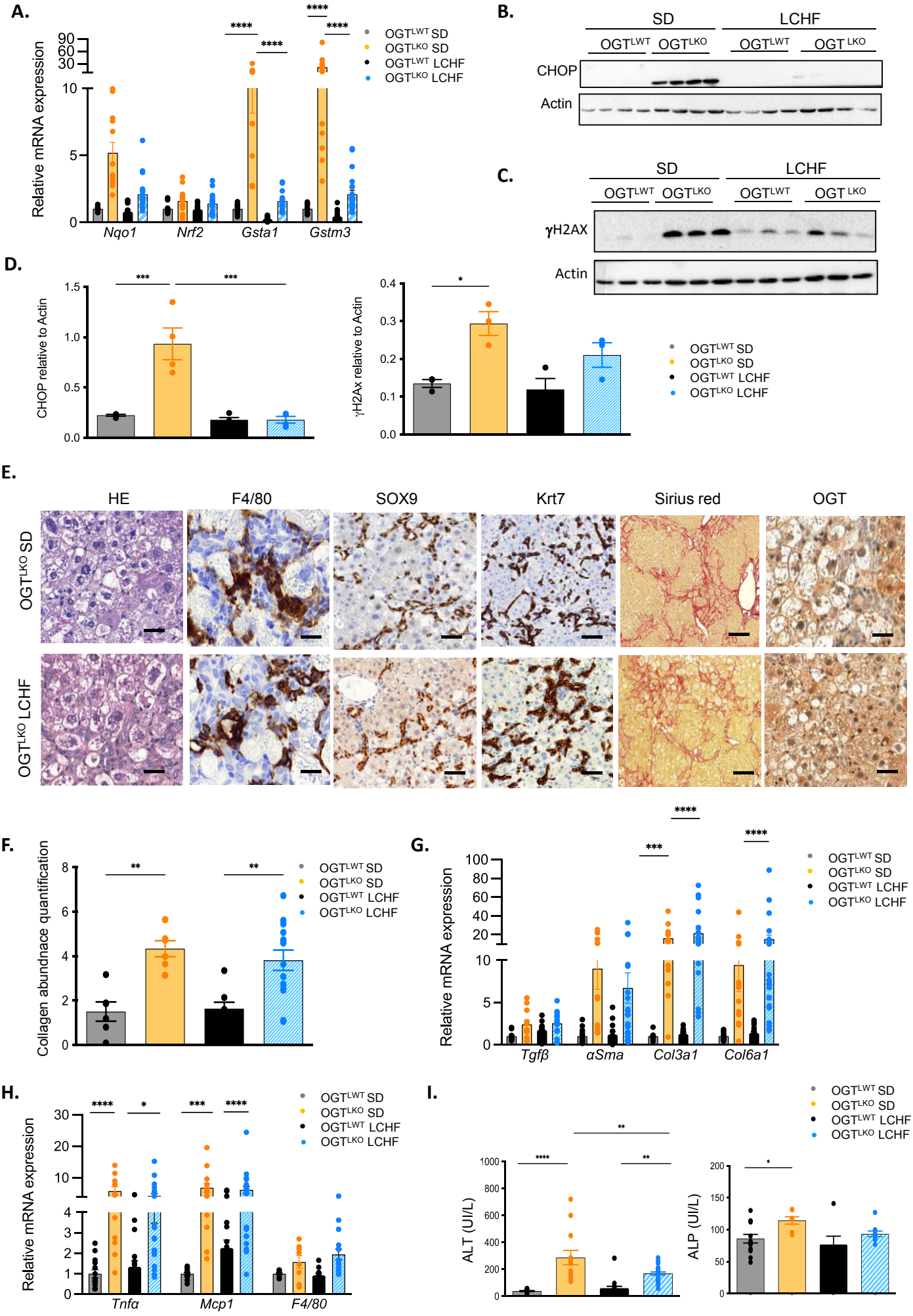
A.
Relative mRNA expression
OGTLWT SD
OGTLKO SD
OGTLWT LCHF
OGTLKO LCHF
Nqo1
Nrf2
Gsta1
Gstm3
B.
SD
LCHF
OGTLWT
OGTLKO
CHOP
Actin
C.
γH2AX
Actin
D.
CHOP relative to Actin
γH2Ax relative to Actin
E.
HE
F4/80
SOX9
Krt7
Sirius red
OGT
OGTLKO SD
OGTLKO LCHF
F.
Collagen abundnace quantification
G.
Relative mRNA expression
Tgfβ
αSma
Col3a1
Col6a1
H.
Relative mRNA expression
Tnfα
Mcp1
F4/80
I.
ALT (UI/L)
ALP (UI/L)

Figure 6

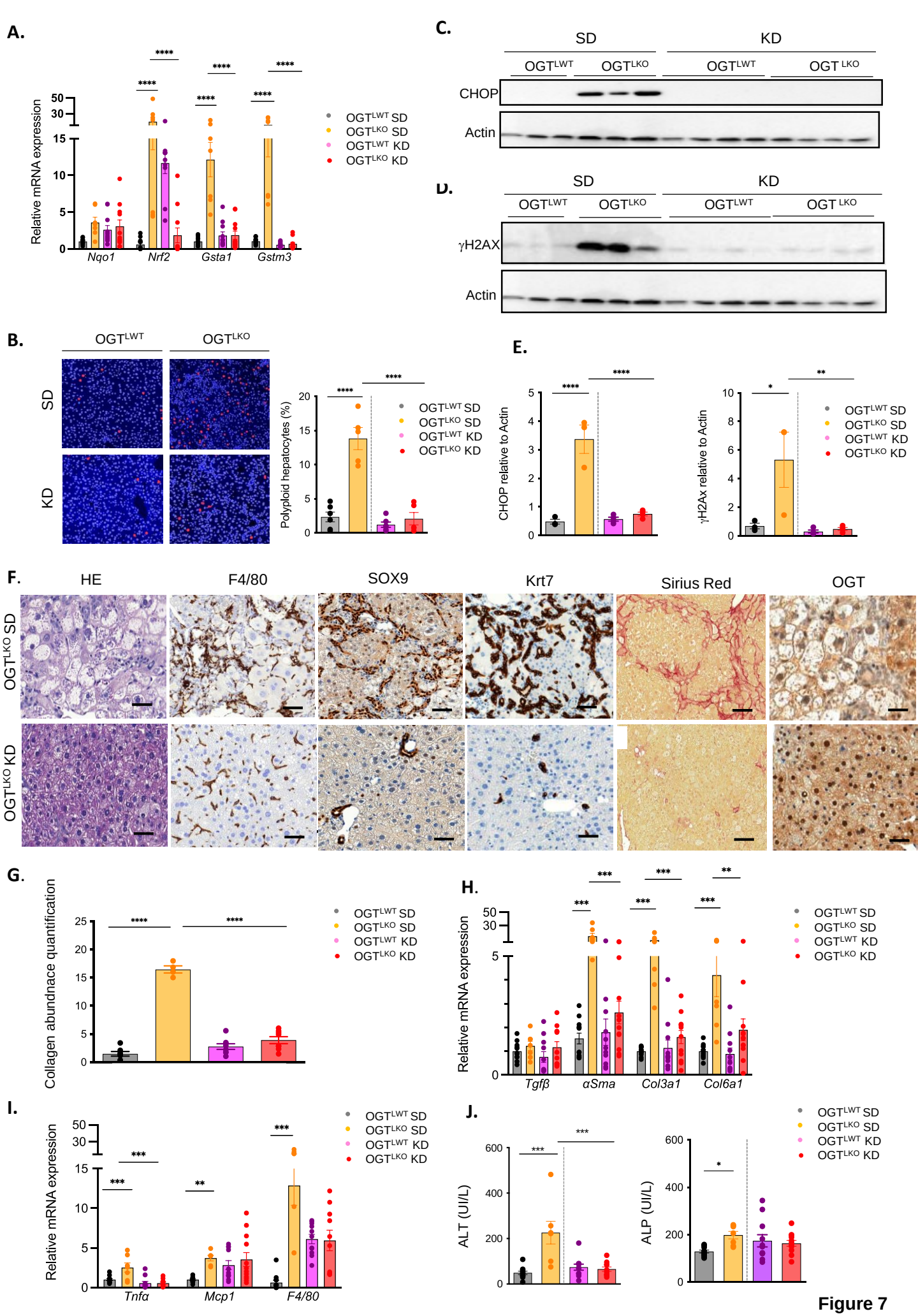
A.
Relative mRNA expression
Nqo1
Nrf2
Gsta1
Gstm3
OGTLWT SD
OGTLKO SD
OGTLWT KD
OGTLKO KD
C.
SD
KD
OGTLWT
OGTLKO
CHOP
Actin
D.
γH2AX
Actin
B.
SD
KD
Polyploid hepatocytes (%)
E.
CHOP relative to Actin
γH2Ax relative to Actin
F.
HE
F4/80
SOX9
Krt7
Sirius Red
OGT
G.
Collagen abundnace quantification
H.
Tgfβ
αSma
Col3a1
Col6a1
I.
Tnfa
Mcp1
F4/80
J.
ALT (UI/L)
ALP (UI/L)

Figure 7

O-GlcNAc transferase acts as a critical nutritional node for the control of liver homeostasis

Paula Ortega-Prieto[1*], Lucia Parlati[1*], Fadila Benhamed[1], Marion Regnier[1], Isadora Cavalcante[2], Mélanie Montabord[1], Rachel Onifarasoaniaina[3], Maryline Favier[3], Natasa Pavlovic [4], Julie Magusto[5], Michèle Cauzac[1], Patrick Pagesy[1], Jérémie Gautheron[5], Chantal Desdouets[4], Sandra Guilmeau[1], Tarik Issad[1]# and Catherine Postic[1]#

[1]Université Paris Cité, Institut Cochin, CNRS, INSERM, Paris, France; [2] Team Genomics and signaling of endocrine tumors, Institut Cochin, CNRS, INSERM, Université Paris Cité, F-75014 PARIS, France ; [3]HistIM Platform, Institut Cochin, CNRS, INSERM, Université de Paris Cité, F- 75014 PARIS, France; [4]Team Proliferation, Stress and liver physiopathology, Centre de Recherche des Cordeliers, INSERM, Sorbonne Université, Université Paris Cité, F-75006 PARIS, France; [5]Centre de Recherche Saint-Antoine, Sorbonne Université, Inserm, Paris, France.

Legends of supplementary Figures

Figure S1. Physiological parameters in 4 week-old OGT^{LWT} and OGT^{LKO} mice. Male liver-specific *Ogt* knockout (OGT^{LKO}) and control floxed littermates (OGT^{LWT}) mice were studied 4 weeks after birth. **A.** Fasting blood glucose (5 hours) (mmol/L). **B**. Glucose tolerance test. The area under the curve (AUC) is shown. **C**. Pyruvate tolerance test. The area under the curve (AUC) is shown. **D**. Insulin tolerance test. The area under the curve (AUC) is shown. **E**. Western blot analysis of Foxo1 (whole lysate), Foxo1O-GlcNAcylation levels (WGA) and global O-GlcNAcylation in liver of OGT^{LWT} and OGT^{LKO} mice. Actin was used as loading control. Three representative samples are presented per condition. **F**. Relative expression levels of gluconeogenic genes normalized to TBP. Data are shown as Mean ± SEM of 6-8 male mice. *P < 0.05; **P < 0.01; ***P<0.001 by unpaired Student t-test (Mann-Whitney).

Figure S2. Liver injury and cell identity assessment in OGT^{LKO} mice. Male liver-specific *Ogt* knockout (OGT^{LKO}) and control floxed littermates (OGT^{LWT}) mice were studied 8 weeks after birth in the fed state. **A**. Relative expression of *Oga* normalized to TBP **B**. Relative expression levels of proliferation markers normalized to TBP. **C**. Western blot analysis of proliferation markers. Three representative samples are shown. Actin was used as a loading control. **D**. Liver section of mice without macroscopic nodular phenotype stained with HE, Sirius red and OGT. **E**. Serum levels of aspartate aminotransferase (AST), total and direct bilirubin and alkaline phosphatase (ALP) in mice 8 weeks after birth. **F.** Representation of hepatoblast differentiation into hepatocytes or cholangiocytes. Markers used for cell characterization are represented under each cellular type. **G**. Relative expression of cell identity markers in livers from OGT^{LWT} compared to OGT^{LKO} mice at 4 and 8 weeks. TBP was used as a housekeeping gene. **H**. Liver sections of 8 week-old mice stained with HNF4α, SOX9 and

Krt19 antibodies. Scale bars = 100 μm on the two upper sections. Detailed zoom is shown in the bottom sections with a scale bar = 50μm. PV: Portal vein. CV: Central vein. Data are represented as Mean ± SEM of 8-10 mice at 4 weeks and 13-15 mice at 8 weeks. **P < 0.01; ***P < 0.001 by unpaired Student t-test (Mann-Whitney) comparing OGT^{LWT} and OGT^{LKO} at the same age.

Figure S3. Female OGT^{LKO} mice exhibit severe liver damage.

Female liver-specific *Ogt* knockout (OGT^{LKO}) and control floxed littermates (OGT^{LWT}) mice were studied 8 weeks after birth in the fed state. **A**. Fed blood glucose (mmol/L), body (g), liver and spleen weights are shown. Liver and spleen weight are represented as percentage of body weight. **B**. Relative expression levels of *Ogt* normalized to TBP. **C**. Western blot analysis of OGT and CHOP protein content in liver of OGT^{LWT} and OGT^{LKO} mice. Four representative samples are shown. Actin was used as a loading control. **D**. Liver sections stained with hematoxylin-eosin (HE), Sirius red, αSMA, OGT, Ki67 and SOX9. Scale bars = 100 μm. **E**. Relative expression levels of inflammatory markers normalized to TBP. **F**. Relative expression levels of fibrosis markers normalized to TBP. **G**. Relative expression levels of oxidative stress markers normalized to TBP. **H**. Serum levels of alanine aminotransferase (ALT). Data are shown as Mean ± SEM of 5 female mice per condition. *P < 0.05; **P < 0.01; ***P < 0.001; ****P<0.0005 by unpaired Student t-test (Mann-Whitney).

Figure S4. Heatmaps of oxidative stress, necroptosis, DNA repair and extracelular matrix.

A. Microarray results of genes involved in oxidative stress. **B**. Microarray results of genes involved in necroptosis. **C**. Microarray results of genes involved in DNA repair. **D**. Microarray results of significant changing genes involved in extracellular matrix formation. Genes found significantly different (either down or up-regulated) between OGT^{LWT} and OGT^{LKO} are

indicated by an asterisk (*). Differentially expressed (DE) gene cut-off was set for a fold change ≥ |2| and False discovery rate (FDR) p-value < 0.05.

Figure S5. Kinetics of inflammation, oxidative stress and ER stress markers in liver of OGT^{LWT} and OGT^{LKO} mice. Male liver-specific *Ogt* knockout (OGT^{LKO}) and control floxed littermates (OGT^{LWT}) mice were studied 2, 4 or 8 weeks after birth in the fed state. **A**. Western blots showing protein content in whole liver lysates of inflammation (Phospho-JNK and total JNK), ER stress (CHOP) markers. Actin and/or HSP90 were used as loading controls. **B**. Relative expression levels of oxidative stress markers and of *Chop* normalized to TBP. Data are represented as Mean ± SEM of 6 mice per group age. *P < 0.05; ***P < 0.001; ****P < 0.0005 by unpaired Student t-test (Mann-Whitney).

Figure S6. Persistent fibrosis and liver injury in 12 weeks and 12 months old OGT^{LKO} mice. Liver-specific *Ogt* knockout (OGT^{LKO}) and control floxed littermates (OGT^{LWT}) mice were studied 12 weeks and 12 months after birth in the fed state. **A.** Liver and spleen weights are shown and are represented as percentage of body weight. **B**. Relative expression levels of oxidative stress and inflammatory markers normalized to TBP. **C**. Liver sections stained with hematoxylin-eosin (HE) and F4/80. Scale bars = 100 µm. **D**. Serum levels of alanine aminotransferase (ALT) of alkaline phosphatase (ALP) and lactate dehydrogenase (LDH). Data are shown as Mean ± SEM of 18-20 individual male and female mice at 12 weeks and 12 months. *P < 0.05; **P < 0.01; ***P < 0.001 and ****P < 0.0005 by unpaired Student t-test (Mann-Whitney).

Figure S7. Low carbohydrate high fat (LCHF) diet improves oxidative stress, ER stress and DNA damage but not fibrosis in OGT^{LKO} mice. A. Liver-specific *Ogt* knockout

(OGT^{LKO}) and control floxed littermates (OGT^{LWT}) mice were weaned (at 3 weeks of age) on a low carbohydrate high fat (LCHF in % of calories: 21% of carbohydrates, 60% of fat, 19% of proteins) diet and sacrificed 5 weeks later in the fed state. **B.** Body weight (g), liver and spleen weights are shown. Liver and spleen weights are represented as percentage of body weight. **C**. Serum concentrations of β-hydroxybutyrate. **D**. Relative expression levels of *Chop* normalized to TBP. **E**. Serum levels of Cxcl1. Data are shown as Mean ± SEM of 4-12 mice (males and females). *P < 0.05; ***P < 0.001; ****P< 0.0005 by unpaired Student t-test (Mann-Whitney).

Figure S8. Ketogenic diet (KD) improves oxidative stress, ER stress, DNA damage, hepatic fibrosis and liver injury in OGT^{LKO} mice. A. Liver-specific *Ogt* knockout (OGT^{LKO}) and control floxed littermates (OGT^{LWT}) were weaned (at 3 weeks of age) on a ketogenic diet (KD: 1% of carbohydrates, 94% of fat, 5% of protein) and sacrificed 5 weeks later in the fed state. **B**. Body weight (g), liver and spleen weights are shown. Liver and spleen weights are represented as percentage of body weight. **C**. Serum concentrations of β-hydroxybutyrate**. D**. Relative expression levels of *Chop* normalized to TBP. Data are shown as Mean ± SEM of 4-8 mice (males and females). ***P < 0.001; ****P < 0.0005 by unpaired Student t-test (Mann-Whitney).

Figure S9. Lipidomic analysis in liver of OGT^{LWT} and OGT^{LKO} mice fed on SD, LCHF or KD diets. A. Heat map of lipid species in liver from OGT^{LWT} and OGT^{LKO} mice fed at weaning for 5 weeks with a LCHF diet. Specific clusters are indicated. **B**. Heat map of lipid species in liver from OGT^{LWT} and OGT^{LKO} fed for 5 weeks at weaning with a KD diet. Specific clusters are indicated. Data are shown as Mean ± SEM of 4-12 mice (males and females).

List of Supplementary Tables

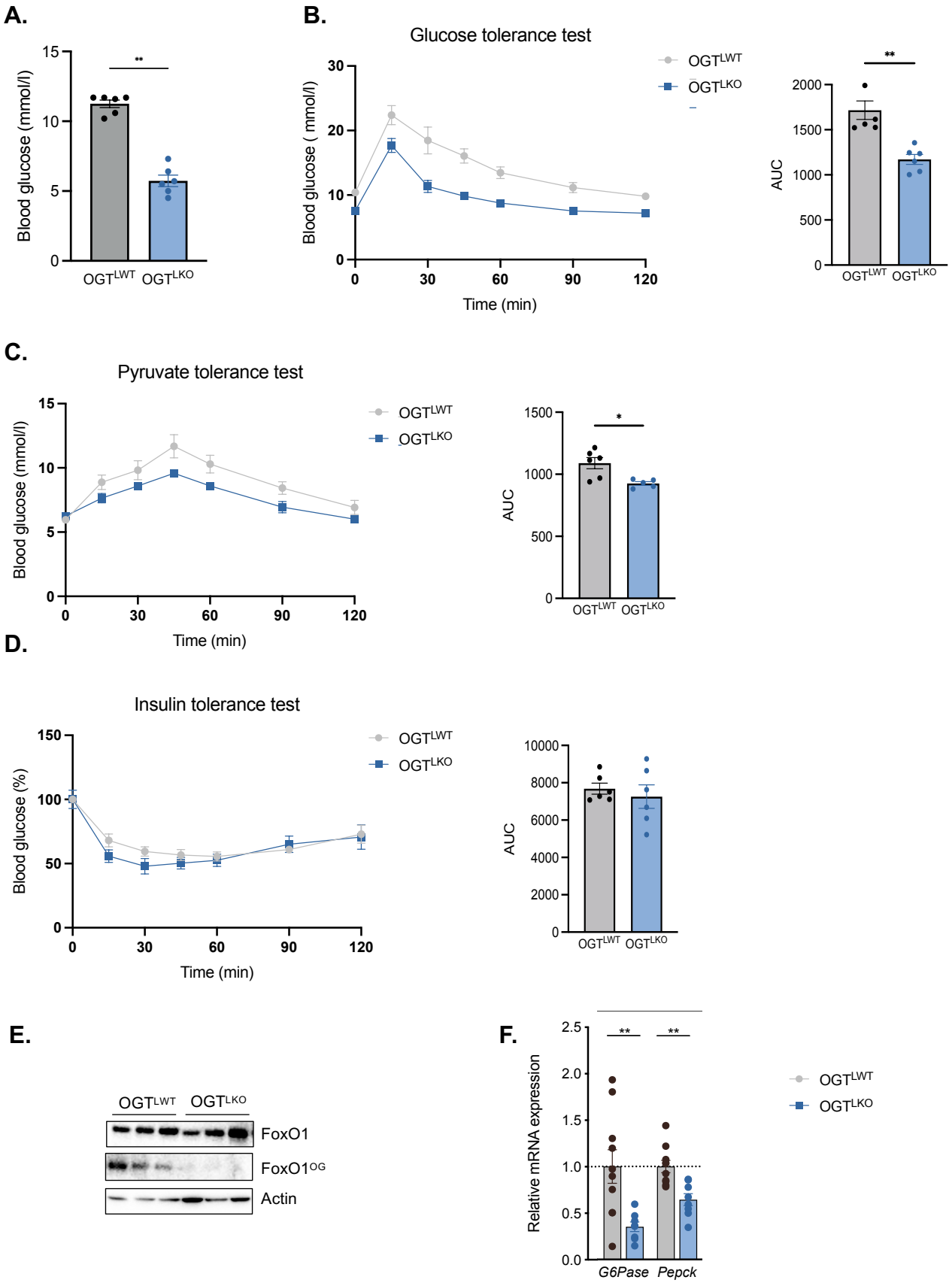
A.
B.
Glucose tolerance test
C.
Pyruvate tolerance test
D.
Insulin tolerance test
E.
F.
Blood glucose (mmol/l)
Blood glucose (mmol/l)
Blood glucose (%)
Time (min)
AUC
OGTLWT
OGTLKO
FoxO1
FoxO1OG
Actin
Relative mRNA expression
G6Pase
Pepck

Figure S1

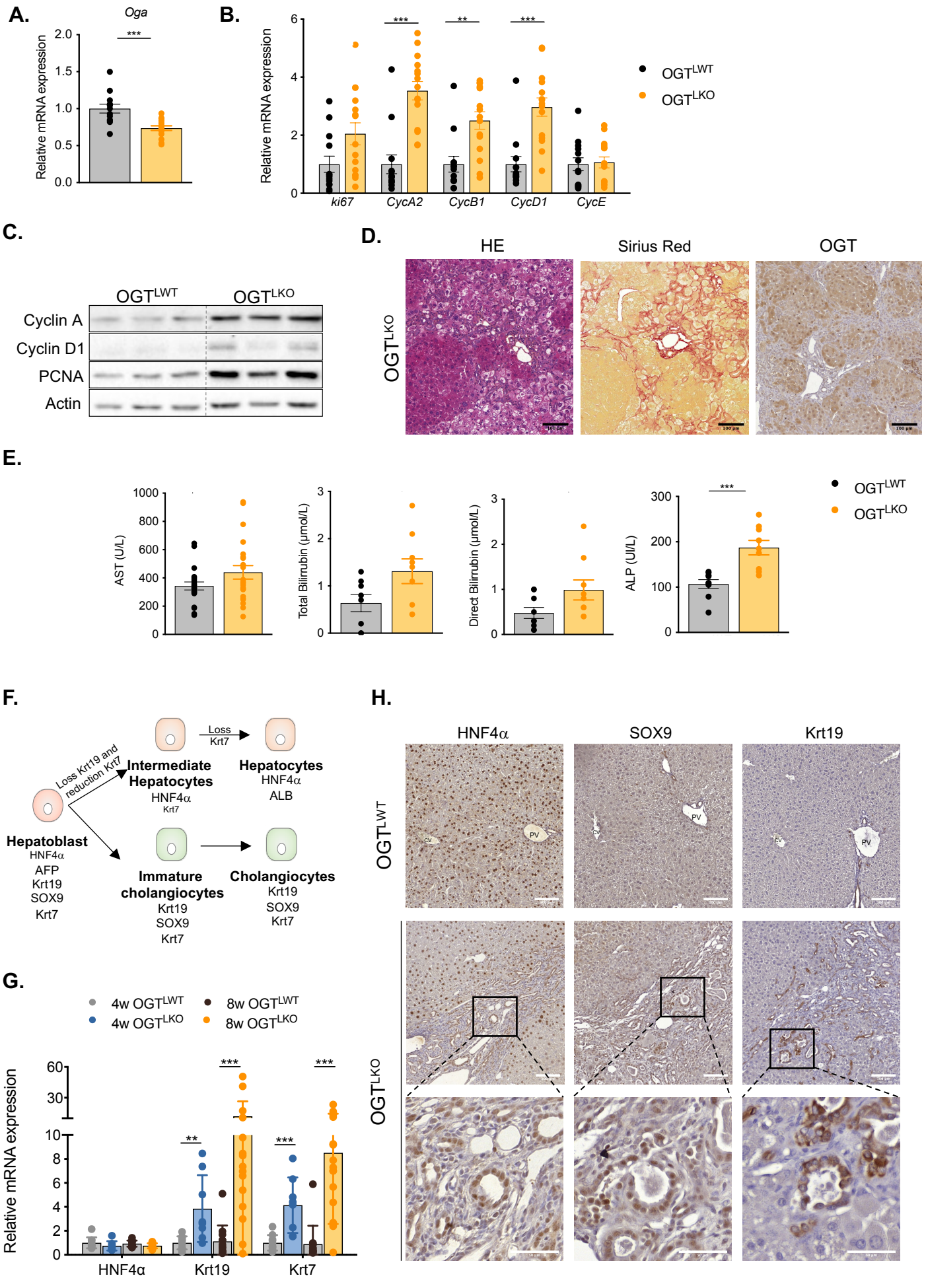
A.
Oga
Relative mRNA expression
B.
Relative mRNA expression
ki67
CycA2
CycB1
CycD1
CycE
OGTLWT
OGTLKO
C.
OGTLWT
OGTLKO
Cyclin A
Cyclin D1
PCNA
Actin
D.
HE
Sirius Red
OGT
OGTLKO
E.
AST (U/L)
Total Bilirubin (μmol/L)
Direct Bilirubin (μmol/L)
ALP (UI/L)
OGTLWT
OGTLKO
F.
Loss Krt7
Loss Krt19 and reduction Krt7
Intermediate Hepatocytes
HNF4α
Krt7
Hepatocytes
HNF4α
ALB
Hepatoblast
HNF4α
AFP
Krt19
SOX9
Krt7
Immature cholangiocytes
Krt19
SOX9
Krt7
Cholangiocytes
Krt19
SOX9
Krt7
G.
4w OGTLWT
4w OGTLKO
8w OGTLWT
8w OGTLKO
Relative mRNA expression
HNF4α
Krt19
Krt7
H.
HNF4α
SOX9
Krt19
OGTLWT
OGTLKO
PV
CV

Figure S2

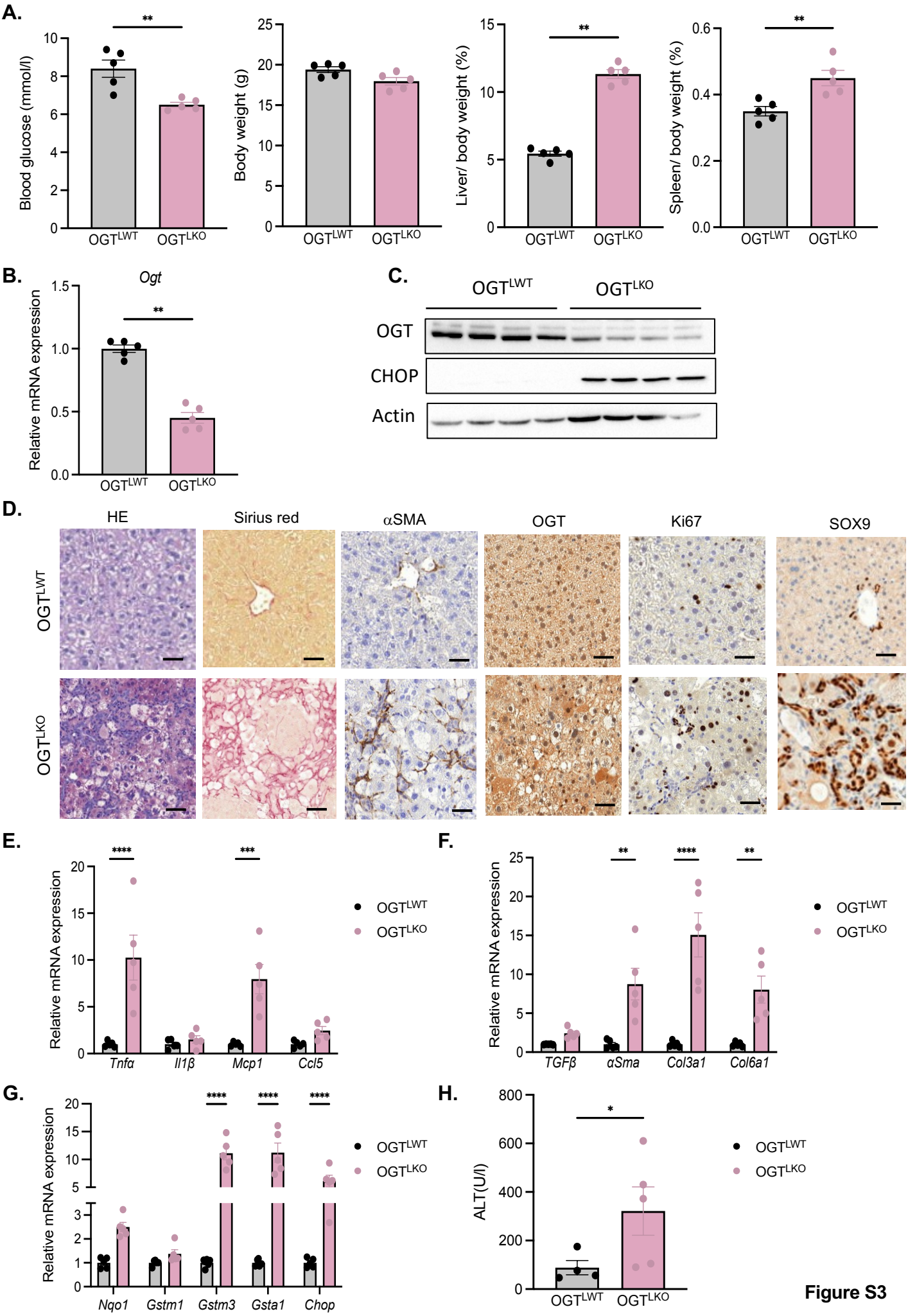
A.
Blood glucose (mmol/l)
Body weight (g)
Liver/ body weight (%)
Spleen/ body weight (%)
OGTLWT
OGTLKO
B.
Ogt
Relative mRNA expression
C.
OGT
CHOP
Actin
D.
HE
Sirius red
αSMA
OGT
Ki67
SOX9
E.
Relative mRNA expression
Tnfα
Il1β
Mcp1
Ccl5
F.
TGFβ
αSma
Col3a1
Col6a1
G.
Nqo1
Gstm1
Gstm3
Gsta1
Chop
H.
ALT(U/l)

Figure S3

A. Oxidative stress

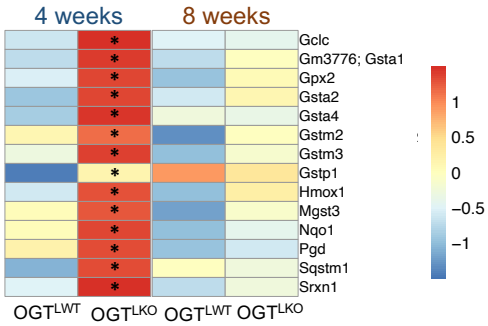

B. Necroptosis

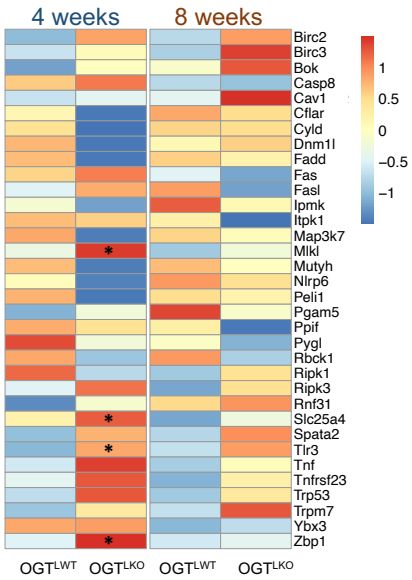

C. DNA repair

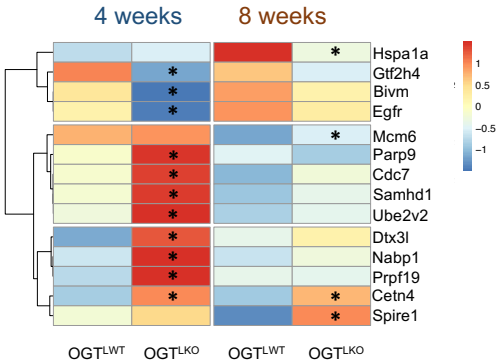

D. Extracellular matrix

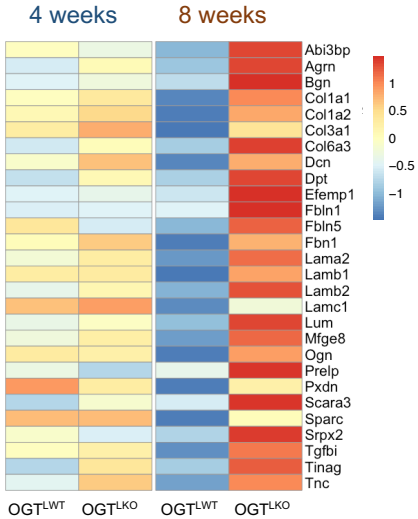

Figure S4

A.

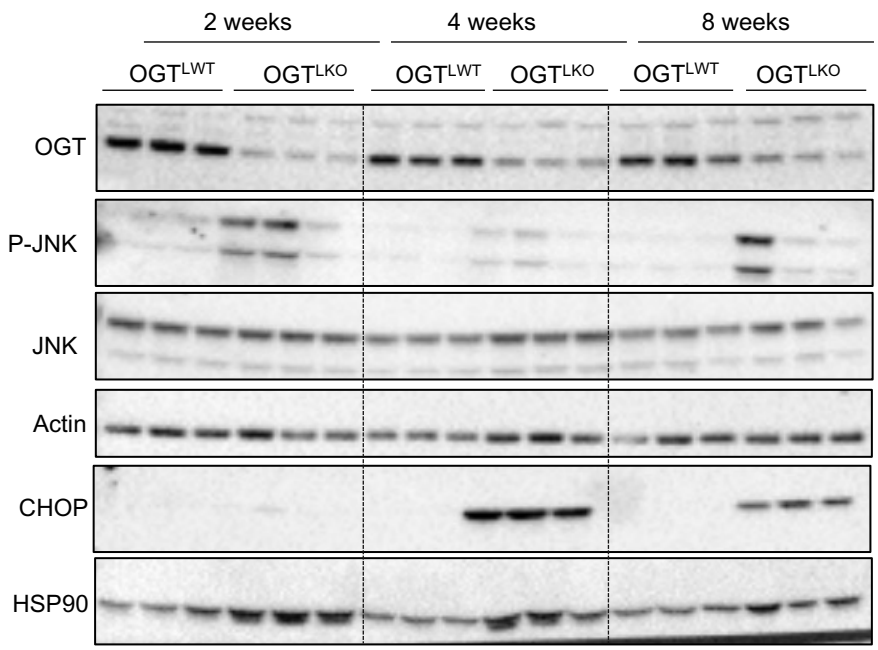
2 weeks
4 weeks
8 weeks
OGT^LWT
OGT^LKO
OGT^LWT
OGT^LKO
OGT^LWT
OGT^LKO
OGT
P-JNK
JNK
Actin
CHOP
HSP90

B.

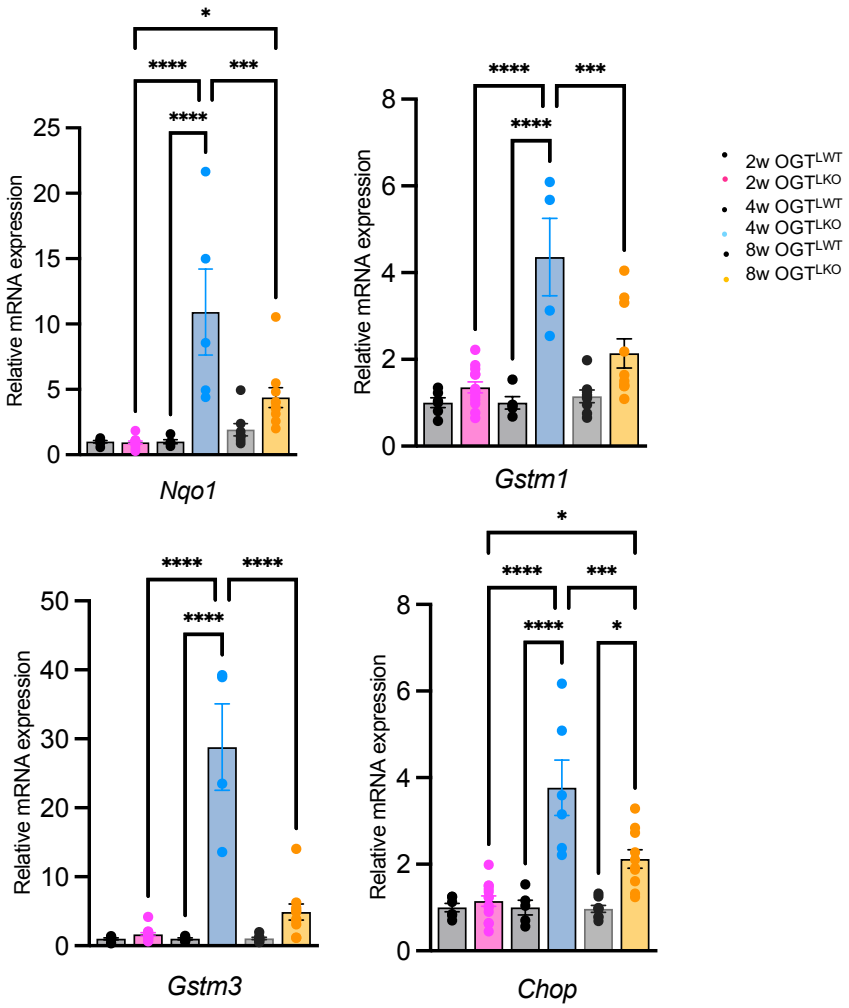
Relative mRNA expression
Nqo1
Gstm1
Gstm3
Chop
2w OGT^LWT
2w OGT^LKO
4w OGT^LWT
4w OGT^LKO
8w OGT^LWT
8w OGT^LKO

Figure S5

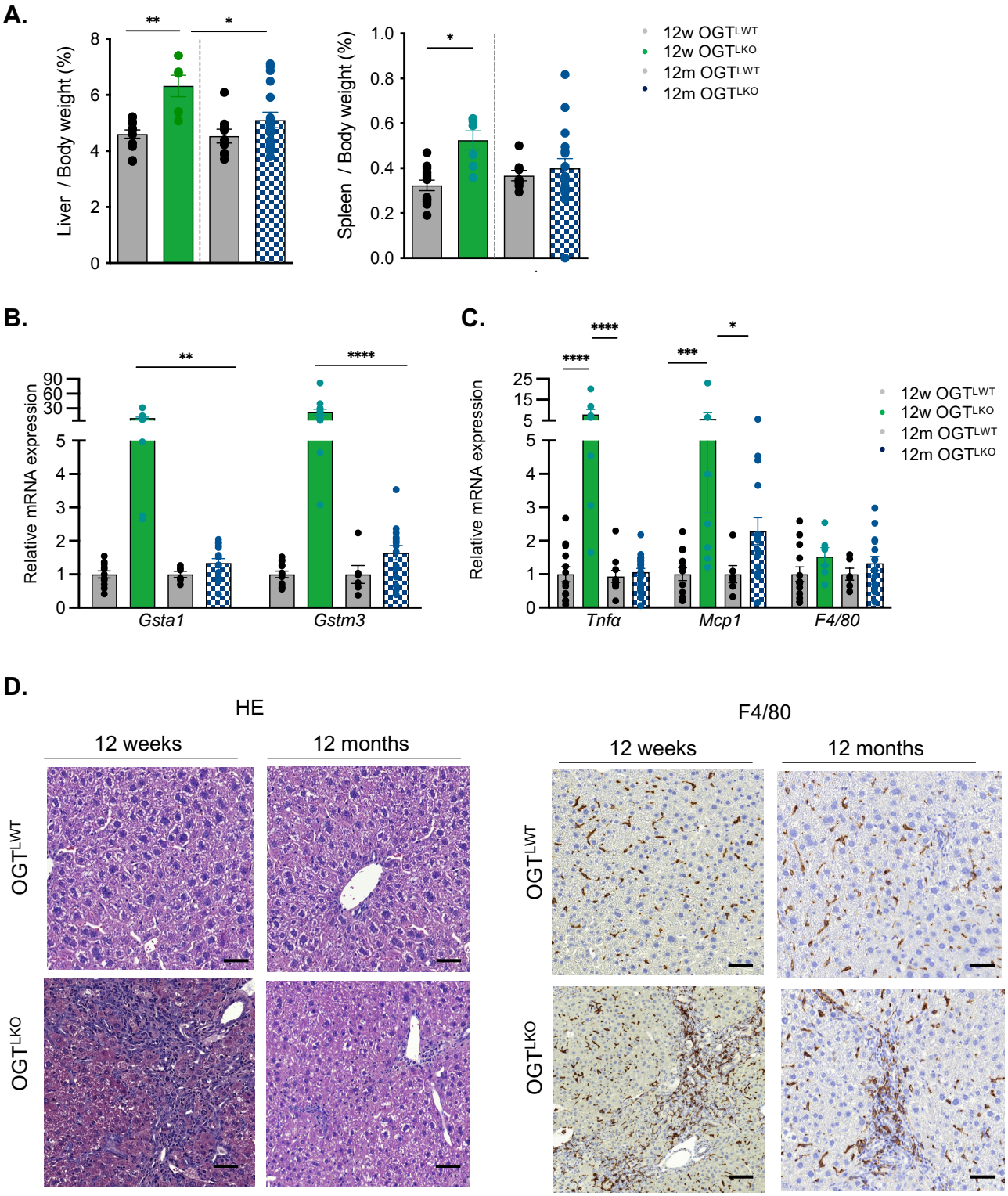
A.
Liver / Body weight (%)
Spleen / Body weight (%)
12w OGTLWT
12w OGTLKO
12m OGTLWT
12m OGTLKO
B.
Relative mRNA expression
Gsta1
Gstm3
C.
Relative mRNA expression
Tnfα
Mcp1
F4/80
D.
HE
F4/80
12 weeks
12 months
OGTLWT
OGTLKO
E.
ALT (UI/L)
ALP (UI/L)
LDH (UI/L)

Figure S6

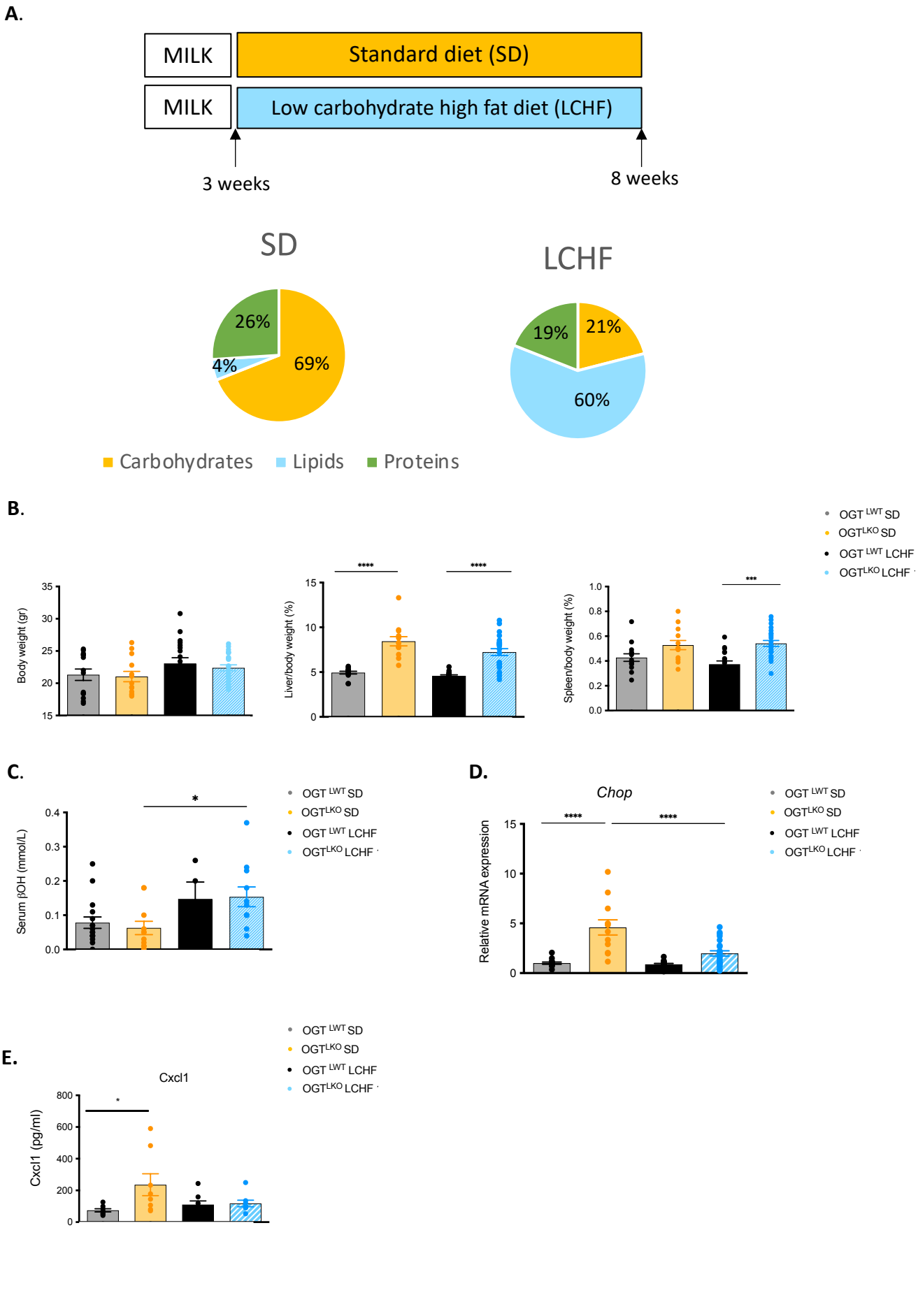
A.
MILK
Standard diet (SD)
MILK
Low carbohydrate high fat diet (LCHF)
3 weeks
8 weeks
SD
26%
4%
69%
LCHF
19%
21%
60%
Carbohydrates
Lipids
Proteins
B.
OGT LWT SD
OGTLKO SD
OGT LWT LCHF
OGTLKO LCHF
Body weight (gr)
Liver/body weight (%)
Spleen/body weight (%)
C.
Serum βOH (mmol/L)
D.
Chop
Relative mRNA expression
E.
Cxcl1
Cxcl1 (pg/ml)

Figure S7

A.

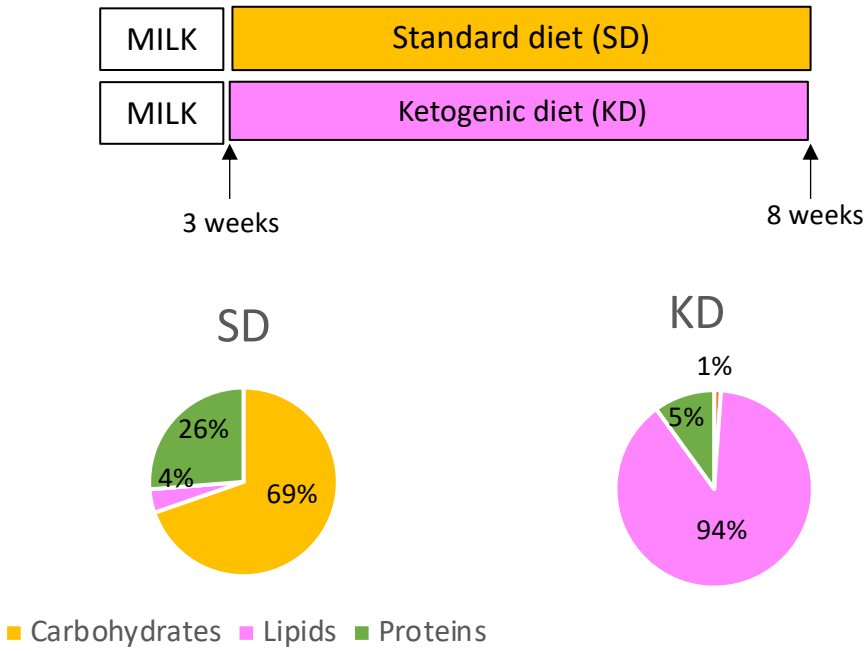

B.

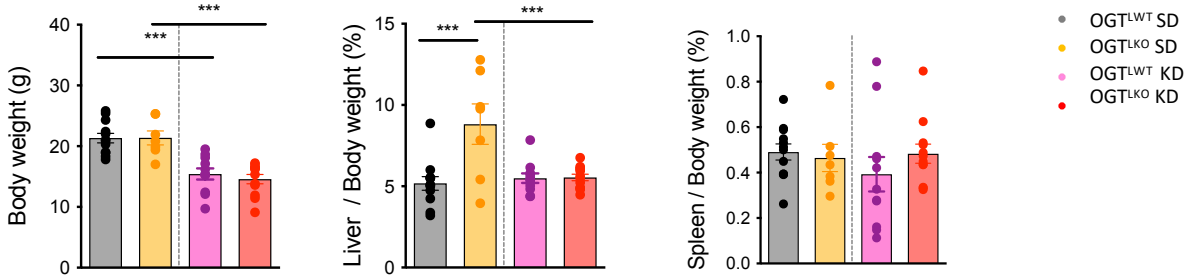

C.

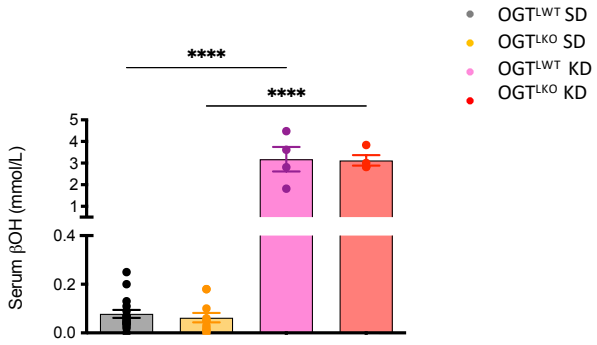

D.

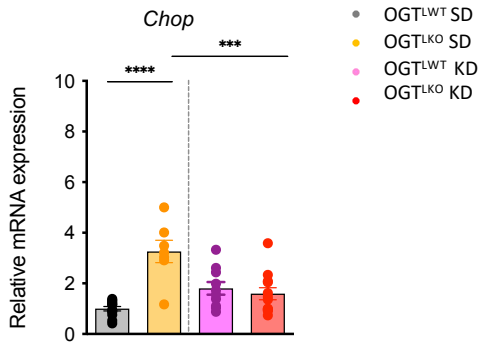

Figure S8

A.

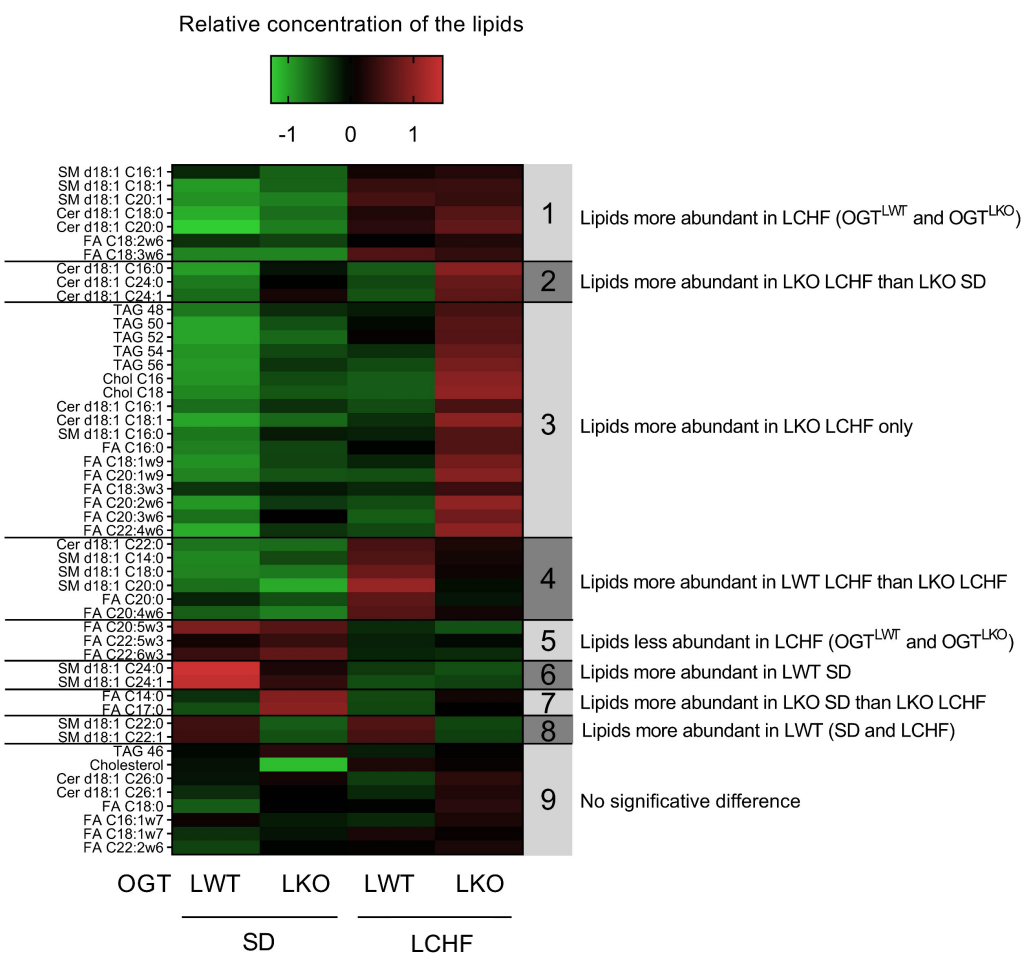
Relative concentration of the lipids
-1
0
1
SM d18:1 C16:1
SM d18:1 C18:1
SM d18:1 C20:1
Cer d18:1 C18:0
Cer d18:1 C20:0
FA C18:2w6
FA C18:3w6
Cer d18:1 C16:0
Cer d18:1 C24:0
Cer d18:1 C24:1
TAG 48
TAG 50
TAG 52
TAG 54
TAG 56
Chol C16
Chol C18
Cer d18:1 C16:1
Cer d18:1 C18:1
SM d18:1 C16:0
FA C16:0
FA C18:1w9
FA C20:1w9
FA C18:3w3
FA C20:2w6
FA C20:3w6
FA C22:4w6
Cer d18:1 C22:0
SM d18:1 C14:0
SM d18:1 C18:0
SM d18:1 C20:0
FA C20:0
FA C20:4w6
FA C20:5w3
FA C22:5w3
FA C22:6w3
SM d18:1 C24:0
SM d18:1 C24:1
FA C14:0
FA C17:0
SM d18:1 C22:0
SM d18:1 C22:1
TAG 46
Cholesterol
Cer d18:1 C26:0
Cer d18:1 C26:1
FA C18:0
FA C16:1w7
FA C18:1w7
FA C22:2w6
1
2
3
4
5
6
7
8
9
Lipids more abundant in LCHF (OGTLWT and OGTLKO)
Lipids more abundant in LKO LCHF than LKO SD
Lipids more abundant in LKO LCHF only
Lipids more abundant in LWT LCHF than LKO LCHF
Lipids less abundant in LCHF (OGTLWT and OGTLKO)
Lipids more abundant in LWT SD
Lipids more abundant in LKO SD than LKO LCHF
Lipids more abundant in LWT (SD and LCHF)
No significative difference
OGT LWT LKO LWT LKO
SD
LCHF

B.

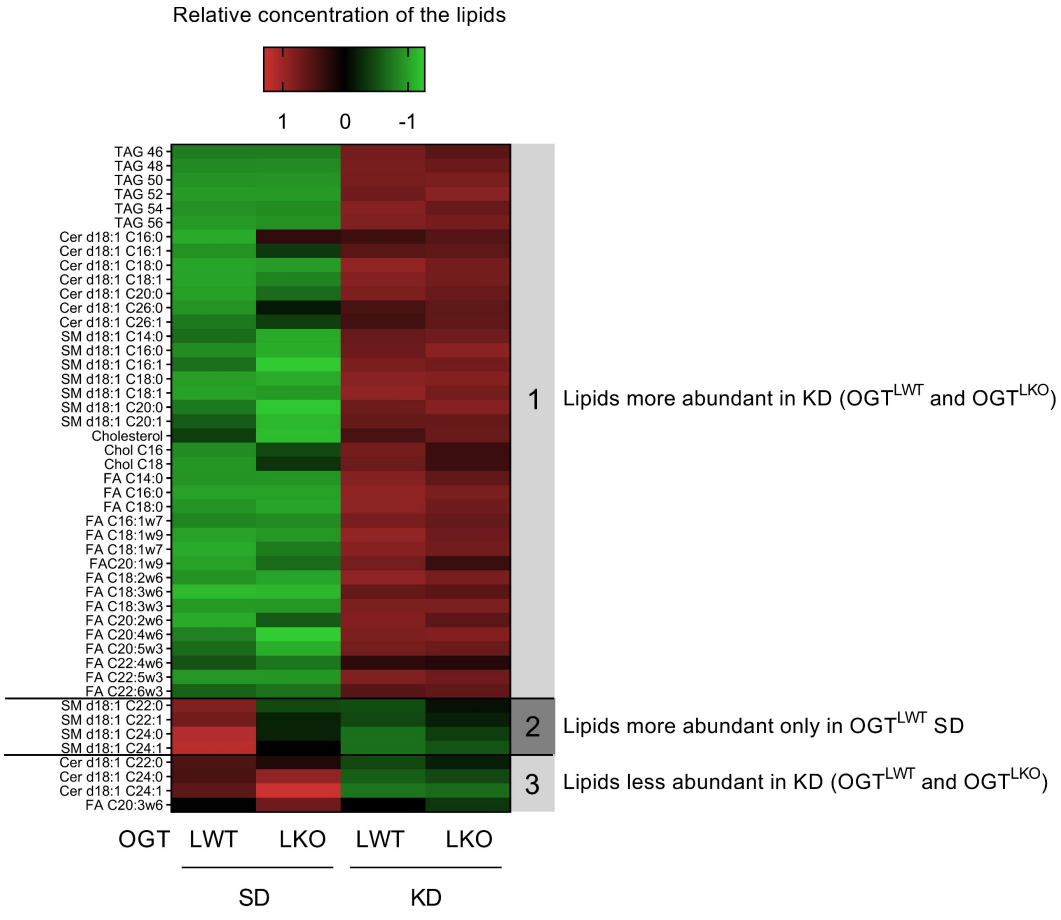
Relative concentration of the lipids
1
0
-1
TAG 46
TAG 48
TAG 50
TAG 52
TAG 54
TAG 56
Cer d18:1 C16:0
Cer d18:1 C16:1
Cer d18:1 C18:0
Cer d18:1 C18:1
Cer d18:1 C20:0
Cer d18:1 C26:0
Cer d18:1 C26:1
SM d18:1 C14:0
SM d18:1 C16:0
SM d18:1 C16:1
SM d18:1 C18:0
SM d18:1 C18:1
SM d18:1 C20:0
SM d18:1 C20:1
Cholesterol
Chol C16
Chol C18
FA C14:0
FA C16:0
FA C18:0
FA C16:1w7
FA C18:1w9
FA C18:1w7
FAC20:1w9
FA C18:2w6
FA C18:3w6
FA C18:3w3
FA C20:2w6
FA C20:4w6
FA C20:5w3
FA C22:4w6
FA C22:5w3
FA C22:6w3
SM d18:1 C22:0
SM d18:1 C22:1
SM d18:1 C24:0
SM d18:1 C24:1
Cer d18:1 C22:0
Cer d18:1 C24:0
Cer d18:1 C24:1
FA C20:3w6
1
2
3
Lipids more abundant in KD (OGTLWT and OGTLKO)
Lipids more abundant only in OGTLWT SD
Lipids less abundant in KD (OGTLWT and OGTLKO)
OGT LWT LKO LWT LKO
SD
KD

Figure S9

TABLE S1. DE genes at 4 weeks

0610010F05Rik	C6	Dhx38	Gcdh
0610011F06Rik	Calml4	Dhx58	Gclc
1110012L19Rik	Car5a	Dixdc1	Gcsh
1700001C19Rik	Car5b	Dlg3	Gde1
1700024P16Rik	Cbr1	Dnaic1	Gdpd1
1810011O10Rik	Cbr3	Dnajc2	Gipc2
2010003K11Rik	Ccbl1	Dnajc4	Gm10639
9130409I23Rik	Ccdc120	Dnpep	Gm10768; Abcc2
A1bg	Ccl19	Dnttip2	Gm11437
Abca3	Ccl2	Dpm3	Gm13139; Znf41-ps
Abcb8	Ccrl2	Dpyd	Gm13248
Abhd14b	Cd200r1	Dtx3l	Gm13251
Abhd15	Cd5l	Dusp10	Gm18853
Abhd6	Cdc7	Dynll1	Gm1966
Acad12	Cdk11b	Ear12; Ear2; Ear3	Gm2a
Acot1	Cdkl5	Echdc1	Gm3776; Gsta1
Acot3	Cenpp	Eda2r	Gm4794
Acot4	Ces1d	Eif2ak2	Gm4952
Acsl1	Ces1e	Eif2d	Gm4955
Acss2	Ces1f	Eif6	Gm7120
Adar	Ces3b	Elovl3	Gm8074
Adgrf1	Cidec	Elp4	Gpi1
Adra1b	Cisd1	Emc10	Gpr155
Afm	Cldn12	Enox2	Gpr35
Afp	Clec2d	Enpep	Gpt
Agpat5	Clpb	Entpd5	Gpx2
AI464131	Cmbl	Epas1	Grb7
Aida	Cmpk2	Epb41l4b	Grem2
Akr1c12	Cmtm6	Ephx1	Gsta2
Akr1c13	Cnnm2	Epsti1	Gsta4
Akr1c19	Cnpy2	Etfdh	Gstk1
Aldh6a1	Coa3	F11	Gsto1
Aph1c	Cops7b	Fabp5	Gstp1
Apol9a	Cox19	Fam131c	Gstp2
Apol9b	Crip2	Fam20a	Gstt1
Apom	Cryz	Fam210b	Gstt3
Apon	Cxcl10	Fam60a	Gtf2h4
Arhgap6	Cxcl9	Fam98a	Gtf2ird2
Arrdc4	Cyp2a22	Fastkd2	Guf1
Aspdh	Cyp2a5; Cyp2a4	Fbxo36	Gvin1
Aspg	Cyp2c40	Fbxo4	Gzmd; Gzme
Asrgl1	Cyp2c69	Fcgrt	H2-Ke6

Atat1	Cyp2d37-ps	Fetub	H2-L; H2-D1
Atf3	Cyp2f2	Fgf21	H2-Q1
Atp2b2	Cyp2j5	Fgfr4	H2-Q4
Atp5e	Cyp2u1	Fhit	H2-Q5
Atp6v1d	Cyp4a31	Foxo1	H2-Q7; H2-Q9
B4galnt1	Cyp4a32	Foxp1	H2-Q8; H2-Q6
Bax	Cyp4f15	Ftsj3	H2-T10
BC021614	Cyp4f17	Fzd8	H2-T22; H2-T9
BC089597	Dapk1	Gabrb3	Hacl1
Bcl2a1a	Dbt	Galnt10	Hao2
Bcl2a1d	Dcxr	Galnt4	Hcfc1r1
Bivm	Ddit3	Gamt	Heatr1
Bmp1	Ddx58	Gbp10; Gbp6	Herc6
Bmp8b	Ddx60	Gbp11	Hes6
Bnip3	Decr2	Gbp2b; Gbp5	Hgfac
Borcs8	Defb1	Gbp3	Hint2
Bphl	Dhx33	Gbp4	Hmox1
Brix1	Dhx37	Gbp9	Hn1

Hpn
Hps4
Hs3st3b1
Hsbp1l1
Hsd11b1
Hsd17b7
Hsd3b1
Hspb1
Hspbap1
Htra2
Hykk
Ifi35
Ifi44
Ifih1
Ifit1
Ifit1bl1
Ifit2
Ifit3
Ifit3b
Igfals
Il22ra1
Il2rg
Impact
Inmt
Irak1; Mir718; Mir5132
Irf7
Irs2
Isg15
Isoc2a
Itih1
Ivd
Kdelc1
Kif3a
Kitl
Klf12
Klf9
Klk1b4
Klkb1; Cyp4v3
Kptn
Krt18
Krt20
Krt8
Mb21d1
Mccc2
Mest
Mgam
Mgea5
Mgll
Mitd1
Mlkl
Mlxipl
Mmab
Mmachc
Mmp13
Mndal
Mpst
Mpv17l2
Mrpl24
Mrpl34
Ms4a4b
Ms4a6b
Msmo1
Mterf3
Mup-ps19; Mup20
Mup20
Mut
Mx1
Mx2
Myc
Myo5c
Myo6
N4bp2
Nabp1
Naglu
Nampt
Ncald; Gm15941
Ndufa3
Ndufaf3
Ndufv3
Neto2
Nit2
Nop56; Snord57
Nqo1
Nr1i3
Pak1ip1
Pank1
Papss2
Paqr9
Parp12
Parp14
Parp9
Pbld1
Pcca
Pccb
Pcid2
Pde9a
Pdk1
Pdxk
Pecr
Peg10
Pex7
Pfdn2
Pgd
Phf11a
Phf11b
Phkg2
Phyhd1
Pik3c2g
Pkd2l2
Pklr
Plek
Pm20d1
Pmvk
Pnpo
Polr3g
Ppfibp2
Ppm1k
Prkra
Prlr
Prodh2
Prpf19
Prpsap1
Prr14
Prss8
Prune
Psmb8
Rars
Rbbp9
Rdh11
Rdh16
Reep6
Rfc2
Rgs1
Rhoc
Rhod
Rnf213
Rnf34
Rock2
Rpn2
Rsad2
Rtp4
Saa3
Samhd1
Scap
Scnn1a
Sec11c
Sell
Selo
Sema4g
Serf1
Serpine2
Serpinf1
Serpinf2
Sesn3
Sfxn1
Sfxn5
Sgsm1
Shb
Shmt1
Slc10a5
Slc11a1
Slc15a3
Slc16a10
Slc16a12
Slc16a2
Slc20a1
Slc22a28
Slc22a30
Sp4
Spats2
Sqle
Sqstm1
Srd5a2
Srxn1
Sstr2
St6galnac6; St6galnac4
Stab2
Stard4
Stat2
Steap2
Stx2
Sult2a8
Sult3a1
Suox
Tcp11l2
Tesk2
Tfdp2
Thoc6
Thtpa; Zfhx2os
Timm21
Tlcd2
Tlr1
Tlr2
Tlr3
Tm2d2
Tmem184c
Tmem256
Tmem43
Tmem53
Tmem97
Tmprss2
Tnfrsf12a
Tnfsf10
Tor1b
Tor3a
Tox
Tprkb
Trim30a
Trim34b; Trim34a
Trmt10a

Lage3	Nr5a2	Psmd5	Slc25a23	Tsc22d3
Lgals3bp	Nrg1	Psmd8	Slc25a42	Tsku
Lilr4b	Nt5dc1	Ptcd3	Slc25a51	Ttc36
Lin7a	Nt5e	Pter	Slc29a1	Ttc38
Lmf1	Nudt19	Ptgr1	Slc35b4	Ttll7
Lonp1	Nudt2	Ptprc	Slc35c2	Uap1l1
Lrp11	Nup133	Pvr	Slc35d1	Ube2v2
Lrrc3	Nup62cl	Pwp2	Slc35e3	Ugdh
Lrsam1	Nxt2	Pxmp2	Slc44a1	Ugp2
Lsg1	Oaf	Pxmp4	Slc47a1	Ugt2a3
Ly6a	Oas1a	Pydc3	Slc4a7	Ugt3a1
Ly6c1	Oas1g	Pydc4	Slc6a12	Ugt3a2
Ly6c2	Oasl2	Pygo1	Slfn5	Ulk2
Lyar	Odf3b	Pyhin1	Slfn8	Uqcr10
Mafb	Ogfrl1	Qdpr	Slpi; Mir7678	Urm1
Man2b2	Ogt	Qsox1	Snrpa1	Uroc1
Map2k6	Orm1	Rab11fip2	Sox6	Usp18
Marchf2	Pafah2	Rabac1	Sp100	Vps28

Vps51; Tm7sf2
Vwa8
Wfdc2
Wfdc21
Wfdc3
Xaf1
Xdh
Yeats4
Yif1a
Zbp1
Zcchc24
Zcwpw1
Zfand4
Zfp65
Zfp729a
Zfp729b
Zpr1

TABLE S2. DE genes at 8 weeks

1600002H07Rik	Atp8a1	Clstn1	Epha3	Gpm6a	Klf6
1700011H14Rik	Axl	Cmtm3	Epha7	Gpm6b	Klhl13
1700047I17Rik2	B4galt6	Cmtm3	Ephx4	Gpr65	Krt19
2210013O21Rik	Bambi	Col1a1	Erich5	Gpx3	Krt7
2610305D13Rik	Bcam	Col1a2	Etl4	Gsn	Lama2
6720489N17Rik	Bcl2	Col3a1	Ets2	Gstm2	Lamb1
Aadat	Bgn	Col6a3	Ezr	Gucy1a3; Mir7010	Lamb2
Abcd2	Bicc1	Cox18	Fam105a	H2-Ab1	Lamc1
Abhd2	C1qb	Cptp	Fam107a	H2-DMb1	Lbh
Abi2	C1qc	Creb3l1	Fam177a	H2-M2	Ldb1
Abi3bp	C1qtnf7	Crtap	Fam180a	Heph	Ldhd
Abr	C3ar1	Csf1r	Fam19a2	Hexa	Lgi2
Ace	Cacnb3	Csrp1	Fam205a2	Hexb	Lgmn
Acot9	Cadm4	Ctgf	Fam47e	Hgf	Lhfp
Acsf2	Capn8	Ctsk	Fbln1	Hist1h2ak	Loxl1
Actg1; Mir6935	Car2	Cttnbp2nl	Fbln5	Hnf4g	Loxl2
Adamts1	Casc4	Cxcr4	Fbn1	Hnrnpa1	Lpar1
Adamts2	Casp12	Cygb	Fcgr3	Hpgds	Lpl
Adamts5	Cav2	Cyp7b1	Fcna	Hsd3b4	Lrrcc1
Adamts9	Cbx6	Cyp8b1	Fermt1	Hsd3b4	Ltbp4
Adamtsl2	Ccdc3	Cysltr1	Fgfr3	Htra1	Lum
Add1; Mir7036b	Ccdc80	D17H6S56E-5	Fgl2	Icosl	Ly86
Adgre5; Mir1668	Ccdc88a	Dab2	Fhl2	Idh2	Lyz2
Adgrg1	Ccnd1	Dcdc2a	Flrt2	Ifi27l2a	Macc1
Adgrg6	Cd14	Dcn	Fmo2	Ifi27l2b	Mamdc2
Adh6-ps1	Cd163	Ddah2	Foxq1	Ifi30	Mamld1
Aebp1	Cd24a	Ddit4l	Frzb	Ifngr1	Map3k1
Agpat4	Cd300lh	Ddr2	Fut10	Ift57	Map4k4
Agrn	Cd300lh	Ddx26b	Fxyd5; Mir7050	Igf1r	Marcks
Ahnak; Mir6367	Cd34	Dkk3	Fzd1	Igfbp3	Mark1
AI506816	Cd36	Dnal1	G2e3	Igfbp7	Mbnl3
Aldh1a2	Cd52	Dock10	G6pdx	Ikbip	Mboat1
Angpt1	Cd68	Dpt	Gabra3	Il10rb	Mcm6
Ankrd1	Cd74; Mir5107	Dpy19l3	Gabrp	Islr	Meis2
Ano1	Cdh6	Dpysl2	Galnt3	Itga3	Mfge8
Ano6	Cdk14	Efemp1	Gas6	Itga8	Mgat4a
Antxr1	Cerk	Efhd2	Gdf10	Itga9	Mid1
Anxa13	Chchd7	Efnb2	Gem	Itgb5	Mir3962
Anxa2	Chst15	Egflam	Gfpt2	Itgb6	Mir6950
Anxa3	Cib3	Ehd2	Gja1	Itgb8	Mir7025
Aoah	Clca3a1; Clca1	Ehf	Gldn	Itgbl1	Mir7677
Apobec3	Clca3a2; Clca2	Elf4	Gm10052	Itm2c	Mmp14

App	Cldn4	Emb	Gm10600	Itpr3	Mmp2
Arg2	Cldn7	Emp1	Gm11710	Itpripl2	Moxd1
Arhgdib	Cldn8	Emp2	Gm11711	Jag1	Mrc2
Arhgef6	Clec4n	Emp3	Gm11711	Jchain	Ms4a4a
Arpc1b	Clic1	Eng	Gm609	Kalrn	Ms4a4d
Art4	Clic6	Enho	Gng2	Kcnma1	Muc1
Atp2b4; Mir6903	Clmp	Enkur	Golm1	Kifc3	Mxra8
Atp6v0d2	Cln6	Epcam	Gpc3	Klf5	Myadm

Mybl1	Pcdhgc3	Rbl1	Tmem229b
Myh9	Pcdhgc4	Rbm3	Tmem45a
Myo1d	Pcdhgc5	Rbms1	Tmem47
Myo7a	Pde1a	Rbms3	Tmsb10
Nav1	Pdgfc	Rbp1	Tmsb4x
Ncam1	Pdgfd	Rcn1	Tnc
Ncoa7	Pdgfra	Rgs2	Tnfrsf19
Ndrg1	Pdgfrb	Rhob	Tns1
Nedd9	Pdzk1ip1	Rhoj	Tns3
Nek5	Pea15a	Rnasel	Tox3
Ngfrap1	Pear1	Robo1	Tpm4
Nipal1	Phactr2	Robo2	Tpr
Nipal2	Phlda1	Rragd	Trib1
Nmnat1	Phldb2	Rtn4	Trove2
Nox4	Pirb	S100a11	Tspan3
Npcd	Pisd-ps3	Scara3	Tspan8
Npr2	Pkd2	Scarf2	Ttc3
Nptxr	Pkhd1	Sccpdh	Tuba1a
Nt5c3b	Plat	Scd2; Mir5114	Ucp2
Nudt7	Pld4	Sdr9c7	Ugt2b38
Obp2a	Plekha2	Selenbp2	Unc5b
Ogn	Plekho1	Selm	Veph1
Olfml3	Plet1	Selplg	Vgll3
Osmr	Plk2	Sema3c	Vim
Pacs1	Plod2	Sema3f	Wbp5
Pam	Plp2	Sema5a	Wfdc15b
Pamr1	Plxdc2	Sema6a	Wls
Parm1	Plxna4	Septin11	Wwc2
Parp8	Ppic	Septin8	Zeb2; Mir5129
Pawr	Ppp1r9b	Serpinb6a	
Pbk	Prelp	Serpinh1	
Pcdhga1	Prex2	Sestd1	
Pcdhga10	Prkch	Sftpd	
Pcdhga11	Prom1	Sh2d4a	
Pcdhga12	Prr15l	Sh3kbp1	
Pcdhga2	Prrg1	Tgfb2	
Pcdhga3	Ptger4	Tgfb3	
Pcdhga4	Ptgfrn	Tgfbi	
Pcdhga5	Ptpn13	Thbs1	
Pcdhga6	Ptpn14	Thbs2	
Pcdhga7	Ptprm	Tiam2	
Pcdhga8	Ptprs	Timp2	

Pcdhga9	Pxdn	Timp3
Pcdhgb1	Rab27b	Tinag
Pcdhgb2	Rab31	Tlr4
Pcdhgb4	Rab8b	Tlr7
Pcdhgb5	Ralgds	Tm4sf1
Pcdhgb6	Rarres1	Tmem106a
Pcdhgb7	Rasef	Tmem173
Pcdhgb8	Rassf9	Tmem189

TABLES3. DE genes common to 4 and 8 weeks

9230110C19Rik	Ifi204
9930111J21Rik1; 9930111J21Rik2	Ifi27
9930111J21Rik2	Iqgap1
Abcb1a	Laptm5
Adora1	Lenep; Flad1
Aebp2	Lifr
AI607873	Lilrb4a
Ajuba	Ly6e
Alcam	Mgst3
Anxa5	Mmp12
Bcl2a1b; Bcl2a1a	Mnda
Capsl	Mpv17l
Ccl22	Ms4a4c
Ccr2	Ms4a6c
Cd180	Ms4a6d
Cd44	Ms4a7
Cd53	Myl12a
Cd63	Myof
Cd9	Nid1
Cetn4	Npnt
Chic1	Ntrk2
Clec12a	P2ry4
Clec7a	Pafah1b3
Csprs	Phf11d; Phf11c
Ctss	Pla2g7
Cxcl16	Plac8
Cybb	Plekhb1
Elovl7	Pygb
Epb41l4a	Retsat
Evi2a; Evi2b; Gm21975	Samd9l
F2rl1	Septin6
Fads3	Sirpa
Fgf1	Slamf7
Flna	Slamf9
Fn3krp	Slc22a26
Glipr1	Slc25a45
Gm13212	Slfn2
Gm2399	Spi1
Gm3934	Tceal8
Gm5431	Tcf24
Gm9844	Tlr13
Gpnmb	Tmem176b

Gstm3
H2-Aa
H2-DMb2
H2-Eb1
Haus8
Hcls1
Ido2
Ifi203
Tmem19
Tnfaip3
Vcam1

TABLES4. Primer sequences

Name	Sequence
Ccl5 F	CTG ACC CTG TAT AGC TTC CCT
Ccl5 R	GGG ATT ACT GAG TGG CAT CC
Chop F	AAG GAG AAG GAG CAG GAG AAC
Chop R	GGT ACA CTT CCG GAG AGA CAG
Col3a1 F	CTGTAACATGGAAACTGGGGAAA
Col3a1 R	CCATAGCTGAACTGAAAACCACC
Col6a1 F	CTGCTGCTACAAGCCTGCT
Col6a1 R	CCCCATAAGGTTTCAGCCTCA
CycA2 F	TGC CTT CAC TCA TTG CTG GA
CycA2 R	TGT GGC GCT TTG AGG TAG GT
CycB1 F	TGC CTT TGT CAC GGC CTT AG
CycB1 R	GGA AAT TCT TGA CAA CGG TG
CycD F	GCG TAC CCT GAC ACC AAT CTC
CycD R	CTC CTC TTC GCA CTT CTG CTC
CycE F	CAGAGCAGCGAGCAGGAGA
CycE R	CAGCTGCTTCCACACCACTG
F4/80 F	CTT TGG CTA TGG GCT TCC AGT C
F4/80 R	GCA AGG AGG ACA GAG TTT ATC GTG
Gpx3 F	GCC ATT TGG CTT GGT CAT TC
Gpx3 R	TGG GGA GTA TCT CCG AGT TC
Gpx4 F	GCA CGA ATT CTC AGC CAA GG
Gpx4 R	CAA ACT GGT TGC AGG GGA AG
Gclc F	CTG CAC ATC TAC CAC GCA GT
Gclc R	TTC ATG ATC GAA GGA CAC CA
Gss F	GAAGCAGCTCGAAGAACTGG
Gss R	AGCACTGGGTACTGGTGAGG
Gsta1 F	CCA GAG CCA TTC TCA ACT A
Gsta1 R	TGC CCA ATC ATT TCA GTC AG
Gstm1 F	CTACCTTGCCCGAAAGCAC
Gstm1 R	ATGTCTGCACGGATCCTCTC
Gstm3 R	TGA AGG CCA TCC CTG AGA AA
Gstm3 F	CTT GGG AGG AAG CGG CTA CT
Gstm5 R	AGA TAC ATC GCA CGC AAG CA
Gstm5 F	CCA TGT GAA TTT CCC CAG GA
Hnf4α F	TGCCTGCCTCAAAGCCAT
Hnf4α R	CACTCAGCCCCTTGGCAT
HO-1 F	GTCAAGCACAGGGTGACAGA
HO-1 R	ATCACCTGCAGCTCCTCAAA
Il-1β F	GGGCCTCAAAGGAAAGAATC
Il-1β R	TACCAGTTGGGGAACTCTGC

KI67 F	AGG ATG GAA GCA AGC CAA CA
KI67 R	GGC CCT TGG CAT ACA CAA AA
Krt7 F	CACCCGGAATGAGATTGCG
Krt7 R	GCACGCTGGTTCTTCAAGGT
Krt19 F	TGCTGGATGAGCTGACTCTG
Krt19 R	AATCCACCTCCACACTGACC
Mcp1 F	TGAATGTGAAGTTGACCCGT
Mcp1 R	AGAAGTGCTTGAGGTGGTTG
Nq01 F	AGC GTT CGG TAT TAC GAT CC
Nq01 R	AGT ACA ATC AGG GCT CTT CTC G
Nrf2 F	TTC TTT CAG CAG CAT CCT CTC CAC
Nrf2 R	ACA GCC TTC AAT AGT CCC GTC CAG
Oga F	TTCACTGAAGGCTAATGGCTCCCG
Oga R	TGTCACAGGCTCCGACCAAGT
Ogt F	TCGCACAGCTCTGTCAAAAA
Ogt R	GCCCTGGGTCGCTTGGAAGA
Phgdh F	GGAGGAGATCTGGCCTCTCT
Phgdh R	GCACACCTTTCTTGCACTGA
αSma F	TGA CCC AGA TTA TGT TTG AGA CC
αSma R	CCA GAG TCC AGC ACA ATA CCA
Tbp F	CCCCACAACTCTTCCATTCT
Tbp R	GCAGGAGTGATAGGGGTCAT
Tgfβ F	TGAGTGGCTGTCTTTTGACG
Tgfβ R	AGTGAGCGCTGAATCGAAAG
Tnfα F	TGGGAGTAGACAAGGTACAACC
Tnfα R	CATCTTCTCAAAATTCGAGTGAC